Dissertations, Master's Theses and Master's Reports

2021

MULTISCALE INVESTIGATION OF DROPWISE CONDENSATION ON A SMOOTH HYDROPHILIC SURFACE

Shahab Bayani Ahangar
Michigan Technological University, sbayania@mtu.edu

MULTISCALE INVESTIGATION OF DROPWISE CONDENSATION ON A
SMOOTH HYDROPHILIC SURFACE

By

Shahab Bayani Ahangar

A DISSERTATION

Submitted in partial fulfillment of the requirements for the degree of

DOCTOR OF PHILOSOPHY

In Mechanical Engineering-Engineering Mechanics

MICHIGAN TECHNOLOGICAL UNIVERSITY

2021

This dissertation has been approved in partial fulfillment of the requirements for the Degree of DOCTOR OF PHILOSOPHY in Mechanical Engineering - Engineering Mechanics.

Department of Mechanical Engineering-Engineering Mechanics

Dissertation Advisor: *Dr. Chang Kyoung Choi*

Committee Member: *Dr. Jeffrey S. Allen*

Committee Member: *Dr. Ezequiel Medici*

Committee Member: *Dr. Jae Yong Suh*

Committee Member: *Dr. Nenad Miljkovic*

Department Chair: *Dr. William Predebon*

Table of Contents

List of Figures

List of Tables

Author Contribution Statement

My PhD research work was supervised by Dr. Chang Kyoung Choi at Michigan Technological University. The work in this dissertation has been published in 4 peer reviewed articles and at least one more article will be submitted in the near future. Out of the 4 published articles, 3 are full length peer reviewed journal publications and 1 is a peer reviewed photogallery entry in the journal of Heat Transfer.

Chapter 1 contains material previously published as literature review in Experiments in Fluids by Ahangar et al. [1].

Chapter 2 contains material previously published in Journal of Flow Visualization and Image Processing by Bayani et al. [2]. My contribution included conceptualization, methodology, visualization, software, validation, formal analysis, investigation, and original writing. The review and edit of the manuscript were a group effort by me, Dr. Chang Kyoung Choi, Dr. Yutaka Tabe, Dr. Yong Tae Kang, and Dr. Seong Hyuk Lee.

Chapter 3 contains material previously published in Experiments in Fluids by Ahangar et al. [1]. Dr. Vinay Kumar Konduru and I were responsible for conceptualization, methodology, visualization, investigation, and software. In addition to these contributions, I was the primary person for formal analysis, validation, all texts, figures, and tables in the manuscript. The review and edit of this article were a group effort by me, Dr. Vinay Kumar Konduru, Dr. Jeffrey Allen, Dr. Nenad Miljkovic, Dr. Seong Hyuk Lee, and Dr. Chang Kyoung Choi.

Chapter 4 contains material previously published in Applied Science by Ahangar et al. [3]. I am the primary author for all texts, figures, and tables. Dr. Fei Long contributed to visualization. The review and edit were a group effort by Dr. Chan Ho Jeong, Dr. Jeffrey Allen, Dr. Seong Hyuk Lee, and Dr. Chang Kyoung Choi.

Chapter 5 contains material that is planned for submission as a letter size article in a peer-reviewed journal. I am the primary author of text, figures, and tables in this chapter.

Acknowledgements

List of Abbreviations

C	offset	α	incident angle (degree)
d	thickness of a layer (nm)	ε	relative permittivity
I	intensity value	η	XPS angle relative to the surface (degree)
K	wave vector (1/nm)	θ	incident angle (degree)
k_0	proportionally constant (molecules/cm2s)	Λ	surface coverage, fraction of surface covered with adsorbed molecules (m2/m2)
k_a	adsorption coefficient	λ	illumination light wavelength (nm)
k_{al}	adsorption coefficient at the liquid-vapor interface	ξ	contact angle (degree)
k_{as}	adsorption coefficient at the solid-vapor interface	ω	uncertainty
K_B	Boltzmann coefficient [1.38E-23 (J/K)]	subscript	
n	refractive index	max	Maximum (at the total internal reflection angle)
P	pressure (Pa)	min	Minimum (at the resonance angle)
r	coefficient of reflection between layers	over	Overlayer
R	gas constant [8.314 (J/mol K)]	SPR	Associated with SPRi
r_a	rate of adsorption (molecules/cm2s)	sub	Sublayer
r_d	rate of desorption (molecules/cm2s)	t	Theoretical
R_{SPR}	SPR reflectance	XPS	Associated with XPS microscopy

S	scaling factor	0	First measurement
T	temperature (°C)	1	Layer 1
w	energy per mole required to evaporate adsorbed molecules (J/mole)	2	Layer 2
w_s	energy per mole required to evaporate adsorbed molecules at the solid-vapor interface (J/mole)	3	Layer 3
w_l	energy per mole required to evaporate adsorbed molecules at the liquid-vapor interface (J/mole)	4	Layer 4
		∞	Thick Au 4f layer with no overlayer

Abstract

The objective of this work is to identify the fundamental mechanism of dropwise condensation on a smooth solid surface by probing the solid-vapor interface during phase-change to evaluate the existence and structure of the thin film and the initial nucleus that develop during condensation. In this work, an automated Surface Plasmon Resonance imaging (SPRi) instrument with the ability to perform imaging in intensity modulation and angular modulation is developed. The SPRi instrument is used to probe (in three dimensions) the adsorbed film that forms on the substrate during dropwise condensation. SPRi with a lateral resolution of ~ 4-10 µm, thickness resolution of 0.1-1nm, and temporal resolution of 200-10,000 frames per second can measure water films that are monolayer to multilayer in thickness. The governing mechanism of dropwise condensation is investigated in detail for stable dropwise condensation on a smooth hydrophilic substrate. The study shows nucleation is the first step in dropwise condensation and no film greater than a monolayer exists between droplets during stable dropwise condensation. Our result confirms previous experimental works in support of nucleation theory as the mechanism of dropwise condensation. Our observation of unstable dropwise condensation of steam on a smooth hydrophilic surface shows presence of a several nanometers thick water film between droplets during dropwise condensation. This data matches with previous experimental work in support of film rupture theory. In summary, our results indicate nucleation theory or film rupture theory may be valid for special experimental settings. And, neither of these two theories are a comprehensive theory than can explain the physics of dropwise condensation.

1 Introduction

Condensation is ubiquitous in many engineering applications and advanced technologies. Examples include power generation [4], air conditioning [5], and thermal management [6, 7]. Condensation of vapor can occur in two modes: film wise and dropwise condensation [8]. In film-wise condensation, a layer of liquid is condensing on a surface. In dropwise condensation, the condensation happens in the form of distinct droplets. Dropwise condensation was first introduced in 1930 by Schmidt et al. [9]. It has been shown that the surface heat transfer coefficient is 4-20 times higher for the dropwise condensation mode [10]. Therefore, it has the potential to improve efficiency and reduce maintenance costs of heat exchanger systems. Dropwise condensation occurs on non-wetting surfaces or partially wetting surfaces [11]. After nine decades of research on dropwise condensation [9, 12-15], the design and fabrication of a surface for industrial application that can sustain this mode of condensation for the long term has not been successful [16-18]. On the engineered surface, after some time droplets join together and make a liquid layer. This layer decreases the efficiency of a thermal system. The main reason behind an unsuccessful design of a surface supporting long-term dropwise condensation is that scientists do not have a united understanding of the physics of dropwise condensation. Therefore, researchers have mostly relied on trial and error to develop new surfaces. On the other hand, research on dropwise condensation over the past century has yielded conflicting experimental results. These conflicting results have complicated understanding of the mechanism of dropwise condensation [19-23]. Several unanswered questions remain about the mechanism of dropwise condensation:

- How do the initial droplets form on the substrate at the onset of condensation?
- What are the factors affecting droplet growth immediately after nucleation?
- Does a thin film exist between discrete droplets?
- Does the area between droplets participate in the overall surface heat transfer?
- What is the coalescence mechanism at nanometric length scales?
- What are the intermolecular forces between the vapor and the substrate?
- How does the wettability and toughness of the substrate affect dropwise condensation nucleation?
- Where does nucleation occur on the substrate?

Currently, there are two major theories on the mechanism of dropwise condensation:

1) Film rupture theory: vapor condenses as a thin film on the surface. At a critical thickness, the thin film breaks up and small droplets form on the surface. According to this theory, a thin film (e.g., a film with a thickness of one monolayer to several molecule layers) covers the substrate. Film rupture theory was first introduced in 1937 by Jacob et al. [24] and since has been supported experimentally by researchers [25].

2) Nucleation theory: droplets nucleate heterogeneously on the surface. Then, the droplets grow and coalesce to make larger droplets. Heat transfer is dominant through the droplets (defined as the active area) and the area between the droplets is considered inactive. The nucleation theory was first introduced by Tammann and Boehme in 1935 [26]. Umur and Griffith [23] showed theoretically there is no film thicker than a monolayer in the inactive area during dropwise condensation. The nucleation theory has been supported experimentally by researchers in the past nine decades. The majority of researchers support nucleation theory as the governing mechanism of dropwise condensation. Numerical models that have been developed to predict dropwise condensation are based on nucleation physics [27].

As Figure 1.1 shows the inability to accurately define the dropwise condensation mechanism is due to the fact that dropwise condensation occurs at various lengths (from an atomistic order at the early stages of drop formation to mesoscale where body forces are important) and at multiple timescales (from bridge formation between two droplets during coalescence that happens in a microsecond to a quasi-steady state of droplet growth that occurs over several seconds). Therefore, a visualization technique that can shed light on the dropwise condensation mechanism needs to have high spatial and temporal resolutions. Also, the technique should be easy to implement in ambient conditions. Optical microscopy [28, 29] and environmental scanning electron microscopy (ESEM) [30-33] are two of the observation techniques that have been reported in the literature for dropwise condensation visualization.

High-speed optical microscopy techniques [28, 29] have a high temporal resolution. Cha, et al. [34] used top-view mode optical microscopy to observe the jumping of a droplet (of a size of hundreds of nanometers) during coalescence at 1,000 frames per second (FPS). The lateral resolution of optical microscopy techniques is limited by the diffraction limit. Another drawback of high-speed optical microscopy is its limited ability to measure film thickness. Optical microscopy techniques, such as fringe equal chromatic order interferometry [35], ultrathin film interferometry [36], and Surface Plasmon Resonance imaging (SPRi) [37, 38] can measure film thicknesses less than 1 μm. Kim et al. [37] used SPRi to provide a 3D map of a thin film with a thickness of less than 400 nm. Still, an optical microscopy technique that can measure sub-nanometer liquid film thicknesses at high-speed (>1,000 FPS) is not available.

In recent years, ESEM has been used to study a variety of complex interfacial phenomena, such as frost formation [39] and dropwise condensation [40]. ESEM can provide dynamic information at a length smaller than a micrometer. It is a perfect tool to investigate drop nucleation sites. Recently, phase reconstruction was proposed to enhance the spatial and temporal resolution of ESEM during dropwise condensation experiments [40]. Currently, ESEM cannot be employed to study the early stages of coalescence because the temporal resolution of this technique is low [15]. Moreover, ultrathin film measurement is challenging using ESEM.
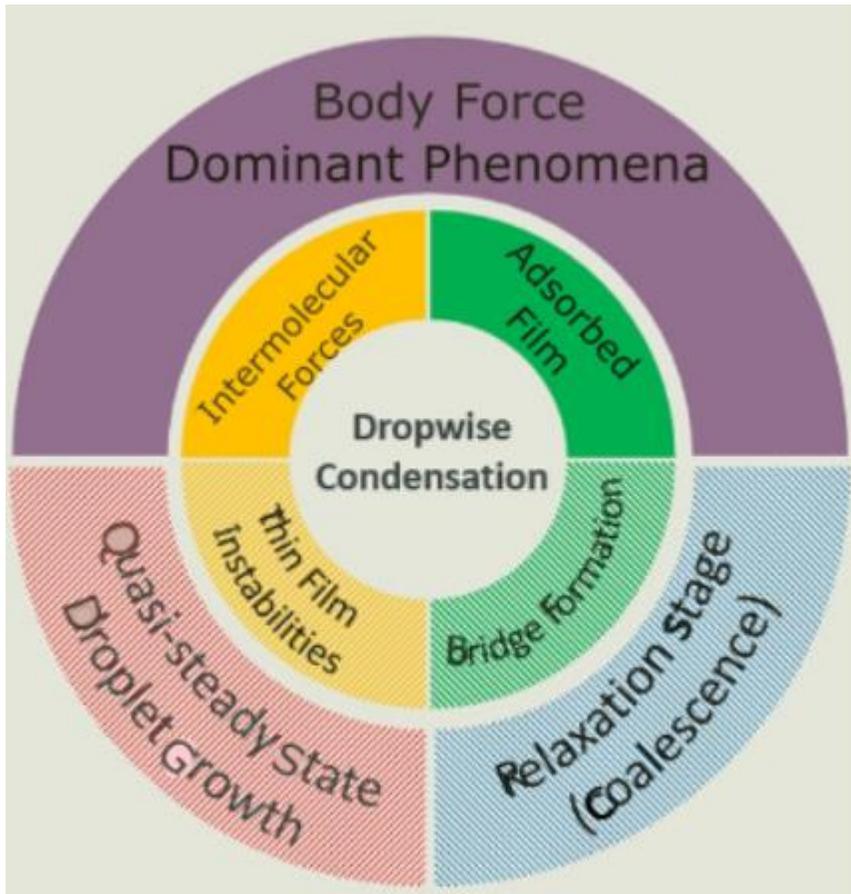
Figure 1.1 Dropwise condensation occurs at various length scales (intermolecular forces, adsorbed film, and body force dominant phenomena) and at various time scales (thin-film instabilities, bridge formation of coalescence, quasi-steady state droplet growth, and relaxation stage of coalescence)

Prior to this work, no microscopic techniques exist with the ability to observe dropwise condensation phenomena at high-speed (more than 200 frames per second) at a sub-nanometer thickness resolution. In this work, automated SPRi is introduced as a tool to study the mechanism of dropwise condensation. SPRi is a label-free imaging technique working based on attenuated total internal reflection. SPRi can detect changes in the Refractive Index (RI) of the test medium in the thin region (<300 nm) above the sensing gold layer. The automated, angle-scanning SPRi instrument was developed by integrating linear and rotating motorized stages. This instrument improves conventional SPRi by enhancing the resolution of angle probing, increasing the speed of angle scanning, and minimizing the angle-dependent image artifacts. The objective of this work is to identify the fundamental mechanism of dropwise condensation on smooth hydrophilic surfaces by atomistically probing the solid-vapor interface during phase-change to evaluate the existence and structure of the thin film and initial nucleus that

develop during condensation. Using experimental and analytical approaches, this study seeks to answer how the first droplets form on the surface during dropwise condensation. Moreover, we study the area between droplets to answer whether a thin film exists between droplets. This works primarily discusses the mechanism of stable dropwise condensation occurring at a low droplet growth rate of 1 µm/s in diameter. Additionally, the work details our observation of unstable dropwise condensation and its effect on the formation of thin-film between droplets.

Chapter 2 contains material previously published in the Journal of Flow visualization and Image Processing by Bayani et al. [2]. It focuses on employing the SPRi as an inexpensive label-free technique to visualize high-frequency feature interfacial phenomena like three stages of coalescence during dropwise condensation. The chapter demonstrates the corresponding image processing method to detect materials on the solid surface. Moreover, it discusses the two techniques shortening the illumination path and broadening a bandpass filter to increase the temporal resolution of SPRi up to 10,000 FPS.

Chapter 3 contains materials previously published in Experiment in Fluids by Ahangar et al. [1]. It focuses on the fabrication and testing of a novel automated angle-scanning surface plasmon resonance imaging (SPRi) instrument. The combination of two stationary mirrors and two angle-controlled mirrors provides high accuracy and high-speed angular probing. This instrument minimizes the angle-dependent image artifact that arises due to beam walk, which is the biggest challenge for the use of SPRi with angular modulation (AM). In the work described in this chapter, two linear stages were employed to minimize the image artifact by adjusting the location of the angle-controlled mirrors and the camera. The effect of the environment's temperature on reflectance during SPRi with intensity modulation (IM) is discussed. This chapter discusses the concept of pixel neighboring to assess the probability of noise and the standard error of thin film measurement. The chapter provides experimental support for the first time on the existent of a molecularly adsorbed water layer that exists between droplets during dropwise condensation.

Chapter 4 contains material previously published in Applied Sciences by Ahangar et al. [3]. It focuses on the effect of adsorbed volatile organic compounds (VOCs) on the ultrathin film measurement using SPRi. Further, the chapter presents the proper surface treatment process that enables the measurement of an ultrathin water layer during high-speed (3,000 FPS) imaging of dropwise condensation. Two methods (1) standard cleaning procedure (SCP) using acetone, isopropyl alcohol, and DI water and (2) SCP followed by air plasma cleaning. It discusses the effect of the cleaning procedures on surface roughness, contact angle, and surface chemistry using Atomic Force Microscopy, optical microscopy, and X-ray photoelectron spectroscope meter. The chapter provides a quantitative analysis on the effect of adsorbed VOCs during dropwise condensation experiments. Specifically, it discusses the composition of a monolayer water film that measured between droplets during dropwise condensation, i.e., how much of the film is made from water and how much of it is made from adsorbed VOCs.

The result of chapter 4 confirms a monolayer water film observation during the dropwise condensation, which has been reported in chapter 3.

Chapter 5 contains material that is planned for submission in a peer-reviewed journal. The chapter focuses on stable dropwise condensation and unstable dropwise condensation. The chapter provides detail on the formation of initial droplets at the onset of stable dropwise condensation. Specifically, the result suggests no film larger than a monolayer exists on the surface. The chapter contains our observation of multilayer thin water film between droplets during unstable dropwise condensation. The chapter suggests the effect of thin film on the degradation of heat transfer rate can be studied quantitatively as future work.

2 Surface Plasmon Resonance Imaging of Drop Coalescence at High-temporal Resolution

The dynamic process at the solid-liquid interface is of vital importance in various phenomena ranging from thin-film instabilities [41], thin-film growth, dropwise frost formation [42], sessile drop coalescence [34], the nucleation-condensation mechanism [43], and spray coating [44]. A variety of imaging techniques, such as environmental scanning electron microscopy (ESEM) [45], atomic force microscopy [46], scanning tunneling microscopy [47], and neutron imaging [48], have been developed to visualize phenomena at the solid-fluid interface.

The instruments mentioned above that are used in the field of interfacial microcopy are considered high-end, expensive, super-resolution microscopes. The need for an expensive microscopic apparatus restricts many laboratories in developing countries from conducting experiments in the field of interfacial sciences due to financial constraints, limited infrastructure, and lack of high-end technical support. Following the notion of portable and low-cost technologies, which is a vision of many researchers, we investigated the application of high-speed surface plasmon resonance imaging (SPRi) for phase-change phenomena. SPRi has been mostly used in investigating low-frequency processes at the interface of solids and fluids, such as measuring the concentration of biomolecules in a solution [49], mapping of slow mixing fluids [50], and mapping of salinity diffusion [51]. The usual temporal resolution for conventional SPRi is less than 240 fps [52]. High-speed SPRi is a recent development for phase-change visualization applications and has primarily been promoted by this group [53-55]. In the present paper, an automated SPRi instrument coupled with high-speed imaging is employed to picture coalescence evolution during dropwise condensation. The automated SPRi platform is made using off-the-shelf components and can be put together and taken apart quickly for storage. This article details the techniques employed to improve the temporal resolution of SPRi and the corresponding image analysis method that can be used to detect materials on the surface of a solid using high-speed SPRi.

2.1 Surface Plasmon Resonance Imaging

SPRi is a technique to visualize nearfield fluidic transports within a few hundred nanometers near a solid surface. This visualization technique works by excitation of free electrons at the interface of a dielectric material and a metal. The typical configuration for an SPR imaging sensor is carried out in a *Kretschmann* arrangement that includes layers of a prism, gold, and test media. When a p-polarized light is launched in different incident angles on the interface of prism-gold through total internal reflection, it transfers energy and momentum to the free electrons. The resonance of free electrons creates an evanescence electromagnetic wave known as surface plasmon polaritons (SPPs) that propagates at the interface of two materials and decays exponentially with distance from the interface. The distance that is the maximum probing length of SPRi depends on the refractive indices and thicknesses of the test media on the gold film. As a result, the intensity of the reflected light from the interface of the prism-gold contains information on the thicknesses and refractive indices of the test media. These two outputs can be decoupled

when image processing based on the corresponding numerical analysis is applied to the SPRi experimental data. The solution of Fresnel's equation for the p-polarized light can predict the SPR reflectance behavior in a four-layer SPR setup:

$$R = \frac{r_{12}[1+\exp(-2ik_2d_2)]+[r_{12}r_{23}+\exp(-2ik_2d_2)]r_{34}\exp(-2k_3d_3)}{1+r_{12}r_{23}\exp(-2ik_2d_2)+[r_{23}+r_{12}\exp(-2ik_2d_2)]r_{34}\exp(-2k_3d_3)}$$
(2.1)

where r_{ij} indicates the coefficient of reflection between the ith and the jth layers, k represents the wave vector, and d is the thickness of a layer. The SPR theory and the steps for deriving equation (1) from Fresnel's equation are discussed in an article by Yamamoto [56]. In our study, subscripts *1, 2, 3*, and *4* represent the BK7 prism, gold film, water, and air, respectively. The thickness of the air and the BK7 prism are considered infinite, and the thickness of the gold film is 50 nm. If there is no water medium, the SPR reflectance changes into a case of three-layers. SPRi can be conducted in different modes, such as angular modulation (AM), intensity modulation (IM), wavelength modulation (WM), and phase modulation (PM) [57]. In this paper, AM and IM are used for recording the images. AM provides imaging at a fixed wavelength by the continuous change of the incident angle. The result is an SPR reflectance curve with the minimum reflectance at an SPR minimum angle, which represents the maximum excitation of SPPs in a test medium. Figure 2.1 shows a typical reflectance curve for air at 550 nm. The SPR minimum angle, i.e., the angle of the minimum reflectance, for air at 550 nm is 46.34°. The most common application of SPRi with AM is measuring the refractive index of a test medium based on the SPR minimum angle. The sensitivity of this method is defined by the ratio of change in the SPR minimum angle ($d\theta$) to the change in the refractive index (dn). The sensitivity can be calculated from the resonant condition for the *Kretschmann* configuration as follows;

$$S_\theta = \frac{d\theta}{dn} = \frac{1}{\sqrt{n_p^2 - n_m^2}}$$
(2.2)

where S_θ is the sensitivity of SPRi with AM, n_p is the refractive index of the prism, and n_m is the refractive index of the test medium. In an imaging system with a BK7 prism and a test medium like water, a change of 2.5×10^{-3} refractive index units (RIU) induces a shift in the SPR minimum angle of 0.2°. SPRi with IM mode is imaging the changes in the intensity of the reflected light at a fixed wavelength and incident angle. This type of SPRi is a perfect mode for high-speed visualization of interfacial phenomena.
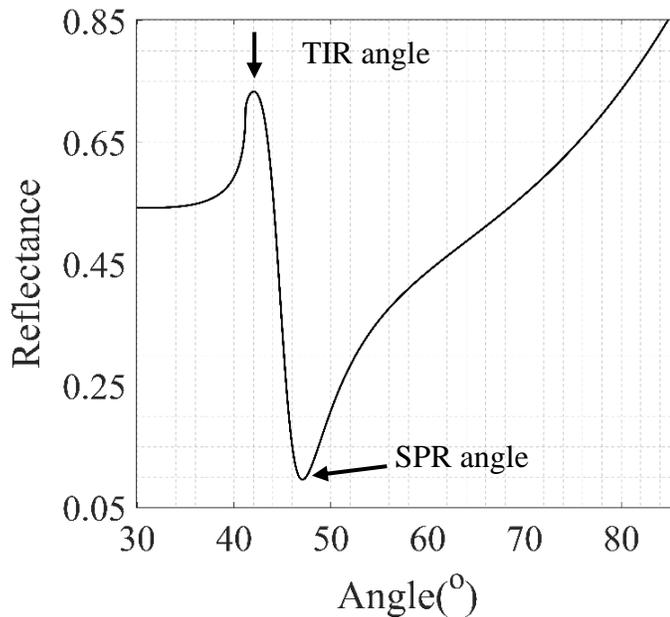
Figure 2.1 SPR reflectance curve of air at 550 nm; Total integral reflection (TIR).

2.2 Experimental Setup

For this project, an automated SPRi instrument capable of AM and IM was built from readily available off-the-shelf components. The microscopy platform was coupled with high-speed imaging to visualize the coalescence during condensation/evaporation experiments. The coalescence process was recorded at 3000 fps and 10000 fps using two different implantations of optical arrays.

2.2.1 SPRi Instrument

The schematic of the SPRi instrument is illustrated in Figure 2.2. The sensing layer was prepared by depositing 2.5 nm of titanium and 50 nm of gold onto cleaned glass slides. The gold-coated glass was attached to a right-angle BK7 prism using an index matching liquid. To produce a quasi-point light source, a light emitted from an LED illumination system was collected and focused by a plano-convex lens on a pinhole with an aperture size of 1.2 mm. A second pinhole with an aperture size of 7 mm was employed to allow the homogeneous part of the light to pass. After the second pinholes, an array consisting of a biconvex lens, a p-polarizer, and a bandpass filter was used to produce a p-polarized collimated light. A setup of a fixed mirror with a 45° orientation and an angle-controlled mirror guided the light from the optical array to the prism. The angle-controlled mirror with a range of 40° enabled fast angle-scanning microscopy to find the SPR minimum angle. A second setup of an angle–controlled mirror and a fixed mirror was used to direct the reflected light from the gold surface to a camera. The APS-RS camera equipped with an Optem 70Xl magnification lens recorded images at high speed. Angle-controlled mirrors mounted on a linear motorized stage were used to follow the beam path during angle-scanning. Finally, the camera was mounted on a motorized linear stage and moved

8

according to a motion function to provide crispy images at each incident angle. The combination of the angle-controlled mirrors and the linear stages allowed the light beam to irradiate at a fixed area of the gold surface during SPRi with AM. An inexpensive Arduino Mega 2560 board was used to control the motorized stages and the camera. The program for controlling the apparatus was developed in the open-source Arduino programming language.
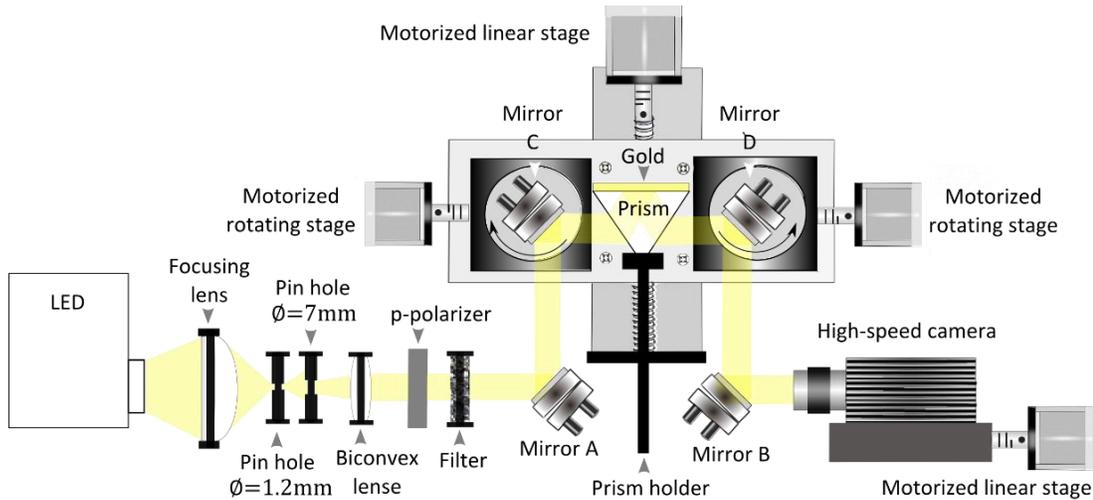
Figure 2.2. Schematic of the automated SPRi instrument.

2.2.2 Condensation/Evaporation Experiment at 3000 FPS

A SugarCube^{TM} – white LED system (Nathaniel Group Inc., Vergennes, VT) was used as the LED illumination system. The optical array that included two pin holes, a p-polarizer, a biconvex lens with the focal length of 150 mm, and a bandpass filter with a FWHM of 10 nm were used to create a p-polarized collimated light. First, the SPR minimum angle of air ($\theta_{air}=46.34°$) was obtained experimentally by sweeping the incident angle from 40° to 70° with steps of 0.2°. Next, the incident angle was adjusted at θ_{air} for SPR imaging with IM at 550 nm. To instigate condensation, four water columns were formed between the gold surface and the ITO-coated glass slide, as shown in Figure 2.3. The ITO was controlled by a laboratory DC power source and was placed 5 mm above the gold surface. When the ITO was heated, the water evaporated from the column and condensed on the gold surface. Time-lapse images were taken from the gold surface at 3000 FPS and a spatial resolution of 4 µm while thermocouples recorded the temperature of the gold surface. The images before the heating of ITO were used as background images in image processing.
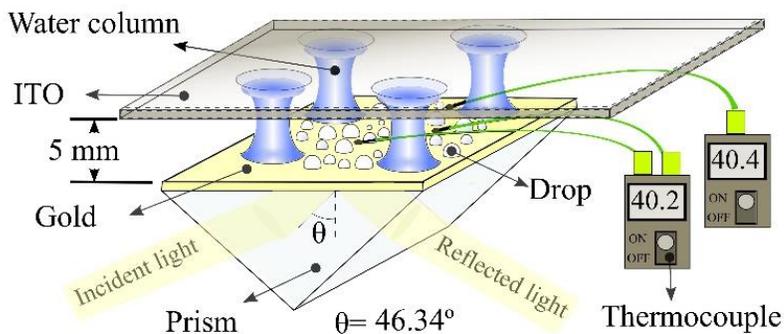
Figure 2.3 Schematic of the condensation experiment.

2.2.3 Condensation/Evaporation Experiment at 10000 FPS

A SugarCube[TM] – Green LED system (Nathaniel Group Inc., Vergennes, VT) with a spectral output range of 450 nm to 620 nm and a center wavelength of 523 nm was employed as the LED illumination system. The bandpass filter was removed from the optical arrays to increase the temporal resolution of the imaging. The experimental procedure to record the coalescence was the same as the one mentioned in the previous section. The SPR minimum angle of air was measured using angle-scanning SPRi. The incident angle was adjusted at the SPR minimum angle of air. Drops coalescence was recorded at 10000 fps and a spatial resolution of 4 µm during SPRi with IM.

2.3 Results and Discussion

2.3.1 Image Processing Method

SPR images are affected by two distinct image artifacts. First, SPR images have an out-of-focus region as the object plane is not parallel with the image plane. In this work, we only studied the focused part of the images. Second, the images are skewed in one of the axes of the x-y plane of the image due to the oblique angle of the gold surface with respect to the objective lens of the camera. Here, image skewness is resolved by multiplying the y-axis of the image plane by $1/\cos(\theta)$, where θ is the incident angle. Figure 2.4 (a) shows the unskewed image.

In the next step of image processing, the time-lapse of background images (12000 frames) were averaged over time to produce a single background image. This background image was subtracted from the condensation images to minimize inhomogeneity in the light and artifacts on the gold surface. Figure 2.4(b) and Figure 2.4(c), respectively, show the background image and the subtracted image. Frame averaging is a conventional noise reduction method in astrophotography [58]. It has been utilized for both low light and high-speed imaging [59]. This method works on the basis that noise in an image behaves randomly. Therefore, oscillations of noise above and below the actual data tend to be even when the number of averaged images increases. Frame averaging minimizes the noise by increasing the signal-to-noise ratio. As true image information remains the same from one frame to the next, this noise reduction method does not suffer from a trade-off with respect to the details of the image, such as sharpness of the image features.
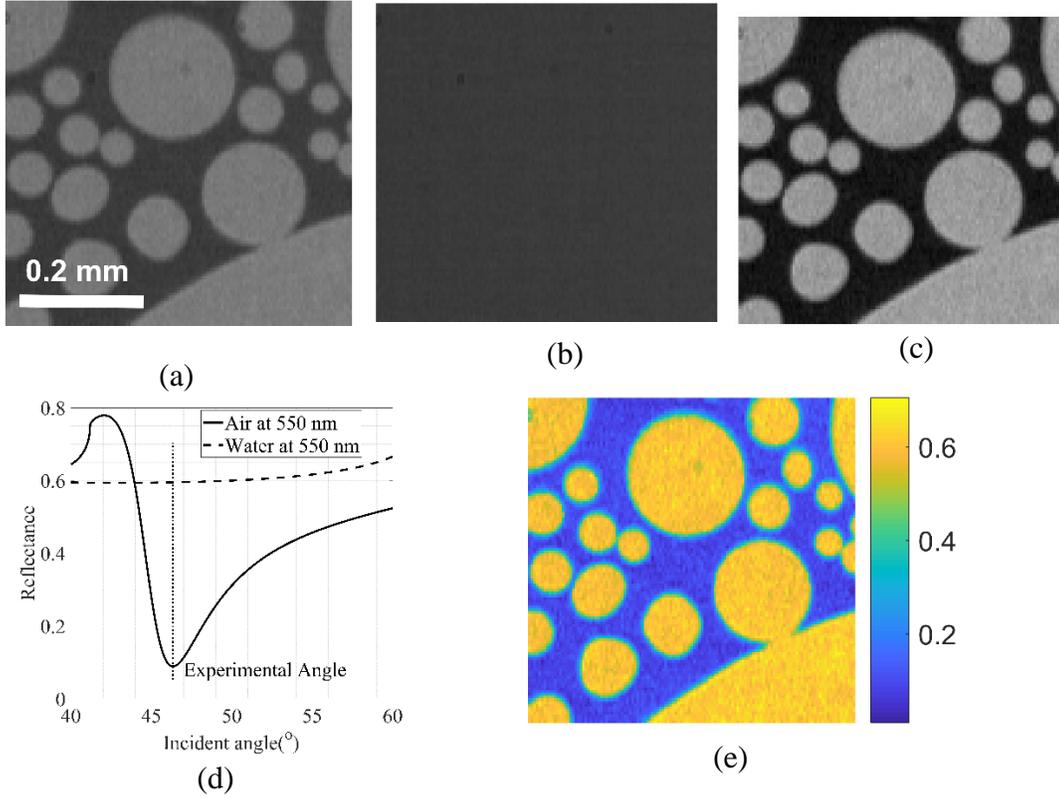
Figure 2.4 Image processing method of high-speed SPRi: (a) SPR raw image with resolved skewness, (b) a modified background image is achieved by frame averaging all of the background images, (c) subtraction of the background image from the raw image to minimize inhomogeneity in light and background, (d) theoretical reflectance for air and water at 550 nm is used to find the scaling factor for image processing, and (e) the color index image with a reflectivity unit is achieved by scaling the subtracted image.

Finally, normalization of condensation images was conducted to change the pixel intensity value to the units of reflectivity (0-1). A normalized image correlates the experimental data to analytical values. The benefit of the normalized image is that it facilitates comparison of different SPR experiments. Moreover, information such as the thickness and the refractive index of a test medium can be deciphered from a color index image. The intensity images are converted to reflectance-based images for quantitative analysis using a calibration factor. The calibration factor is calculated as:

$$S = \frac{I_{max} - I_{min}}{Ref_{max} - Ref_{min}} \qquad\qquad (\ 2.3\ )$$

I_{max} and I_{min} represent maximum and minimum intensity from the intensity-angle curve obtained from angle scanning SPRi. Ref_{max} and Ref_{min} indicate to the theoretical maximum and minimum reflectance in the reflectance-angle curve, as shown in Figure 2.4(d). Knowing the calibration factor, the intensity of each pixel can be converted using the following equations:

11

$$\mathrm{C} = I_{max} - S * Ref_{min} \qquad\qquad (2.4)$$

$$R_{SPR} = (I - C)/S + Ref_{min} \qquad\qquad (2.5)$$

where *I* is the pixel intensity value, R_{SPR} is the pixel reflectance, and *C* is the offset. At the fixed angle (θ= *46.34°*) of the SPRi with IM, materials on the substrate have distinct reflectance numbers that can be attributed to their refractive indices and thicknesses. This data can be used to map the materials on the sensing surface. Figure 2.4(e) shows the color index image achieved using the image processing method. The blue color represents air, and the yellow color indicates water. When more than two materials exist on the surface, for example, in the case of frost formation with the simultaneous presence of ice, liquid, and vapor, three distinct colors represent the three phases of water in the processed image. A similar image processing routine can be employed to map the thickness of the test medium on the surface [14].

2.3.2 Effect of Shortening the Illumination Path

In high-speed SPRi, the signal level depends on several factors including the frame rate of imaging and the degree of light collimation. Increasing the frame rate in SPRi is possible by shortening the exposure time of each frame to the object. A shorter exposure time can be achieved at the expense of signal level. On the other hand, perfect collimation is only possible when an infinitesimal point source is placed at the focus point of the collimator lens. In reality, this scenario is not possible. Besides, even if this scenario is met, the produced optical power would not be sufficient for imaging at a high frame per second (fps) rate. In a typical SPRi with LED as the illumination system, optical arrays create a quasi-collimated light that disperses with distance. Hence, shortening the illumination path can increase the signal level required for high-speed SPRi.

In our previous work [55], we showed SPRi of coalescence at 1500 fps when a biconvex length with a focal length of 500 mm was used in the optical arrays. Here, a biconvex lens with a focal length of 150 mm was employed to minimize the illumination path. By shortening the distance between the first pinhole and the collimator lens from 500 mm to 150 mm, the temporal resolution was improved from 1500 fps to 3000 fps.

2.3.3 Effect of Broadening the Bandpass Filter

Typically, the SPRi platform with an LED illumination system employs a narrow bandpass filter. The spectral transmittance of a bandpass filter is in the form of a Gaussian distribution. Figure 2.5(a) shows the transmittance of the 523nm bandpass filter with FWHM values of 1, 10, and 40 nm. Figure 2.5(b) illustrates the spectral output of the SugarCube[TM] – Green LED illumination system, which is very close to the Gaussian distribution with a peak at 523 nm and FWHM of 60 nm. It is intuitive that the optical power of the unfiltered illumination system is larger than the optical power of the illumination system with a narrow bandpass filter. This is because an unfiltered illumination light can enhance the temporal resolution of imaging. Since equation (1) predict the SPR reflectance in response to a p-polarized monochromatic light, it is necessary to study the effect of polychromatic light on the SPR reflectance behavior.
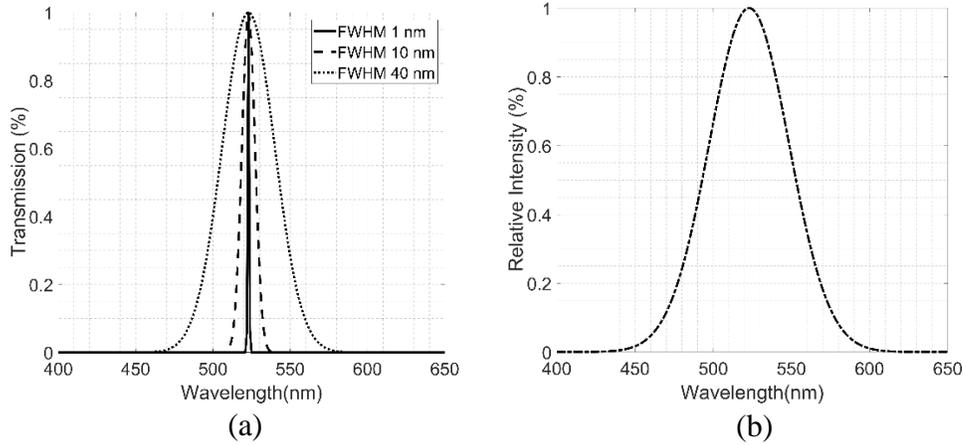
Figure 2.5 (a) Theoretical Spectral transmittance of a 523 nm bandpass filter with FWHM of 1, 10, and 40 nm and (b) Spectral output of Sugar Cube-Green LED.

Figure 2.6 represents the theoretical plot of the SPR reflectance curve for FWHM values of 1, 10, 40 nm and unfiltered green light. The simulation was completed using the Fresnel equation for 3-layer mediums- BK7, gold, and air. A weighted average of the solution considered the effect of the bandpass filter at each wavelength by the following equations:

$$R_b = \frac{\int R \; \varphi(\lambda) \, \gamma(\lambda) \, d\lambda}{\int \varphi(\lambda) \, \gamma(\lambda) \, d\lambda} \qquad\qquad (2.6)$$

$$\varphi(\lambda) = \frac{2.7724}{FWHM} \exp\left(-(\lambda - \lambda_0)\right) \qquad\qquad (2.7)$$

where R_b is the effective SPR reflectance, $\varphi(\lambda)$ is the Gaussian distribution function of the bandpass filter, $\gamma(\lambda)$ is the Gaussian distribution function of the illumination system, λ is the wavelength, and λ_0 is 523nm- peak excitation wavelength. In case of no bandpass filter $\varphi(\lambda)$ is considered as one. The result shows the bandpass filter with the FWHM of 10 nm has a reflectance curve nearly identical to the monochromatic light. However, it has more optical power and can provide a higher signal level. Therefore, filter with FWHM of 10 nm is the most popular filter in SPRi. When broader bandpass filters are used in SPRi, the reflectance curve diverges from the SPR response of the monochromatic light. In our SPRi instrument, imaging at 10000 fps is practical when the unfiltered green light with an approximate FWHM of 60 nm is employed as the illumination system; however, the level of reflectance deep-shift decreases by 14.5 %, compared to the SPR reflectance curve of the monochromatic light. This drop in the level of reflectance minimizes the sensitivity of the SPRi instrument. The broadening of a light also causes chromatic aberration in the image due to dispersion. In the case of our experiments, broadening the bandpass filter from 523 nm with a FWHM of 10 nm to a FWHM of 60 nm does not substantially affect our image features. Moreover, it is worthy to note that the change of the LED system from Sugar Cube-white to Sugar Cubes-Green did not have a significant impact on the temporal

resolution. SPRi with IM at 10000 fps enabled us to visualize the details of coalescence evolution during dropwise condensation.
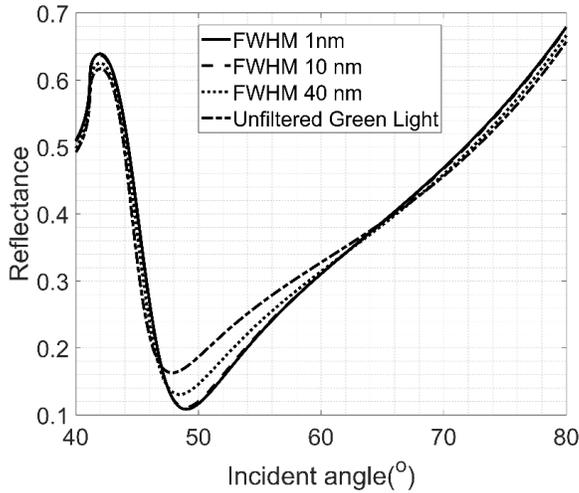
Figure 2.6 Theoretical SPR reflectance in a 3-layer system - BK7, metal, and air- excited by a Gaussian bandpass filter with peak excitation of 523 nm and FWHM values of 1, 10 and 40 nm compared with the unfiltered Sugar Cube-green light-Gaussian distribution with peak excitation of 523 nm and FWHM of 60 nm.

2.3.4 Coalescence Evolution

Figure 2.7 shows three steps of coalescence recorded at 10,000 FPS. Initially, a bridge forms between two droplets and the width of the bridge increases at a high velocity. The length of the bridge is less than the size of the smaller droplet. During bridge evolution, no significant contact line motion can be observed in locations farther from the bridge. The first stage of coalescence happened at less than 0.3 ms in the example case shown in Figure 2.7. In the second stage of coalescence which happens at the time scale more extensive than the duration of bridge formation, two droplets move and merge to develop a peanut-shaped composite droplet. In this stage, the contact line motion is maximum. If the sizes of droplets are close to each other, both of droplets move to form a larger droplet. Otherwise, the larger droplet has no substantial motion, and the smaller droplet moves toward the larger droplet. The timescale of the second stage of coalescence depends on the sizes of the two droplets and varies from 3 to 60 ms. In the coalescence case depicted in Figure 2.7, the second stage took 14.2 ms to complete. The last stage of coalescence, known as the relaxation stage, the contact line of the droplet (periphery of the droplet) moves very slowly until the composite droplet reaches its equilibrium condition. This final stage of drop coalescence can take 0.1~2 s, depending on the sizes of the two droplets. The relaxation stage was complete in less than a second from the initiation of coalescence in the example case represented in Figure 2.7. As it is hard to visualize the displacement of the composite droplet during the second and third stages in the example case, the displacements of the droplet during these two stages are depicted in Figure 2.8. The bright color in Figure 2.8(a) represents the area that the new droplet swept on the substrate during

14

the second stage of coalescence. The image is created by subtracting the image at t= 14.5 ms from the image at t=0.3 ms. Figure 2.8(b) shows the swept area on the gold surface by the composite droplet during the relaxation stage of coalescence that occurred between t=14.5 ms and t=889.5 ms.
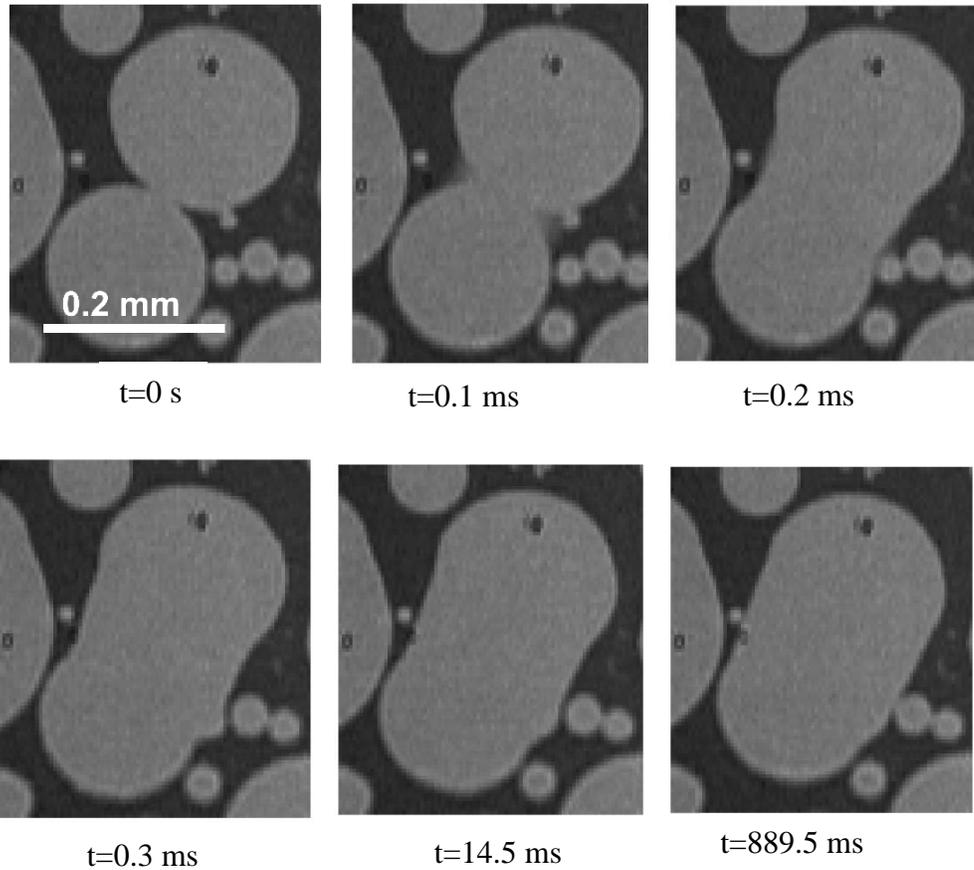
Figure 2.7 Time sequence of droplet coalescence recorded at 10,000 fps (scale bar is 0.2 mm): the coalescence starts by forming a bridge between two droplets (t is less than 0.3 ms), the two droplets move toward each other to form a composite droplet (t is less than 15.4 ms), and the boundary of the composite droplet moves very slowly until the droplet reaches an equilibrium condition.

Dynamics of drop coalescence have been studied mostly using optical microscopy techniques. Wang et al [60] showed 3 stages of coalescence using a top-view optical microscopy at a temporal resolution of 30000 FPS and a spatial resolution of 46 µm. Our proposed SPRi technique has a lower temporal resolution but a finer spatial resolution, compared to this optical microscopy technique. The advantages of SPRi over the optical microscopy techniques are SPRi's real-time measurements of test medium thickness and accurate mapping of the features at the solid-liquid interface in the image. The shadowing effect may interfere with the ability of optical microscopy techniques to accurately detect the edges of the features in the image.

(a)   (b)
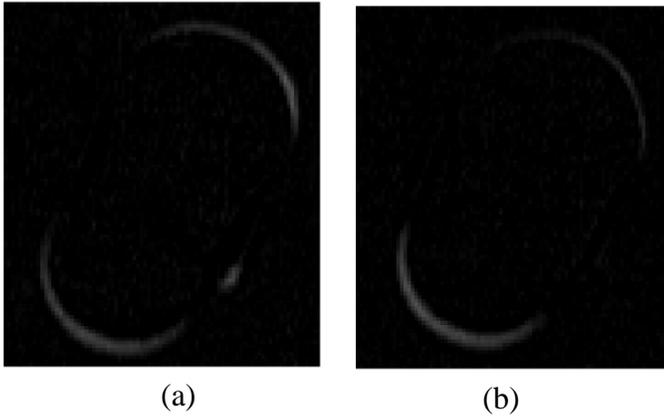
Figure 2.8 (a) The bright gray is the area which has been swept by the droplet during the second stage of coalescence (the image is produced by subtracting the image at t =14.4 ms from the frame at t = 0.3 ms) and (b) the bright gray shows the area which has been swept by the droplet during the relaxation stage of coalescence (t =14.5 ms to t = 889.5 ms).

2.4 Conclusion

The SPRi described in this paper can accurately detect the liquid-solid interface; thus, it has the potential to be considered as a powerful microscopy technique for the high-speed visualization of phase change phenomena. In this work, an inexpensive, tabletop, automated SPRi system capable of imaging with AM and IM is introduced. Moreover, visualization of drop coalescence during dropwise condensation is presented as a model case. The image processing method proposed to accurately identify phases on the substrate is discussed. In this imaging technique, the intensity-based image is converted to reflectance unit images for material labeling. Two methods to increase the temporal resolution of SPRi with IM are discussed. The short-illumination path method uses the collimator lens with a short focal length to minimize dispersion in the illumination system and hence improve the optical power of the incident light. The broadening method uses polychromatic light to intensify the SPR signal level at the receiver. Although broadening the bandpass filter can boost the temporal resolution of the imaging, it sacrifices the sensitivity of the SPRi system. Analytical studies using the Fresnel equation for a multilayered system show broadening the green light (523 nm) from a FWHM of 10 nm to a FWHM of 60 nm drops the sensitivity by 14.5 %. In the visualization of coalescence, the temporal resolution is improved from 1500 fps [55] to 10,000 FPS when a short-illumination path and broadening methods are employed. The three stages of coalescence – bridge formation, contact line motion, and relaxation – can be observed using SPRi at 10,000 FPS. Owing to the improvement of the temporal resolution in SPRi, for the first time high-frequency phase change phenomena like coalescence are observed via a microscopy technique that is different from optical microscopy methods.

16

3 Development of Automated Angle-scanning, High-speed Surface Plasmon Resonance Imaging and SPRi Visualization for the Study of Dropwise Condensation

Condensation is ubiquitous in industrial applications and advanced technologies [4, 6, 61-67]. It has been shown that a substrate that supports dropwise condensation has a higher heat transfer rate compared to filmwise condensation [10]. However, sustainable dropwise condensation for industrial application has not been successful [68]. The main reason is that the physics behind dropwise condensation is not fully understood [27].

Currently, there are two competing theories on the mechanism of dropwise condensation: film rupture theory and classical nucleation theory [69]. In film rupture theory, it is hypothesized that a thin film initially forms on the substrate. At a critical thickness larger than a monolayer, the thin film breaks up and small droplets form on the surface. Conversely, nucleation theory claims that droplets nucleate heterogeneously on the surface. Nucleation theory assumes that droplets grow by direct condensation of vapor on the liquid-vapor interface, and no film greater than a monolayer exists between discrete droplets.

Given the lack of direct microscopic techniques with the ability to observe dropwise condensation at multi length-scales and time-scales, novel experimental methods should be developed to enable a better understanding of dropwise condensation. Previously, we reported that SPRi can be implemented to visualize phase change phenomena [2, 67, 70]. The goal of this chapter is to introduce a newly developed automated SPRi instrument that can be used for quantifying sub-nanometer film at the high-temporal resolution of 3,000 FPS during dropwise condensation.

3.1 Surface Plasmon Resonance Imaging

SPRi is a label-free optical technique that can detect small changes in the refractive index of a dielectric medium near a metal surface [71]. This method has been used widely to detect biomolecular interactions [72]. SPRi, or surface plasmon resonance (SPR) microscopy developed from total internal reflection microscopy, was first introduced by Rothenhäusler and Knoll [73]. In principle, SPRi can be used to measure optical properties of dielectric [74], film thickness [37], and surface coverage [75] on a substrate in a dielectric environment. SPRi has been adapted for studding near-field characterization of fluid flows [50, 76].

SPR theory can be explained using quantum mechanics and electrodynamics principles. Surface plasmons are oscillations of free electrons at the interface of a dielectric material and a noble metal (such as silver or gold). In SPRi, the surface plasmons are excited optically through the attenuated total internal reflection (ATIR). The most widely used sensor setup for excitation of surface plasmons is based on prism coupling using the Kretschmann configuration; in this setup, incident light comes through the prism and is

reflected at the metal layer [77]. The electronic excitation results in a drop in the intensity of reflected light. The angle of an incident light at which the maximum drop in the intensity of light occurs is known as the SPR minimum angle.

The intensity of the reflected light depends on several factors, including wavelength, incident angle, polarization, number of mediums above the surface, and refractive index of the mediums. Hence, different SPRi techniques have been developed, such as angular modulation (AM), polarization modulation (PM), wavelength modulation (WM), and intensity modulation (IM). The AM technique has the highest sensitivity for material characterization [78]. In the AM approach, the intensity of the light reflected from the dielectric medium/metal interface is measured at a constant wavelength through continuous scanning over the incident angles. The result is an angular spectral curve of the test medium that can be used to find the optimum angle for IM microscopy. Therefore, a high-precision angular microscopy platform is required for SPRi. The biggest challenge for high-precision SPRi with AM is the angle-dependent image artifact [79]. This artifact, beam walk, arises because the footprint of a beam on the metal substrate spatially transits at each incident angle. Therefore, the surface features move in the recorded images. Beam walk usually occurs in SPRi instruments with an equilateral prism mounted on the rotating stage. As in this SPRi instrument, the prism is rotated to create different incident angles and the beam translation on the surface causes a shift in the position of features inside the beam, and, consequently, in the recorded images.

The conventional AM approach uses a goniometer with a manual rotating stage [80]. This technique suffers from three main issues: low precision in angle probing, slow angle scanning, and angle-dependent image artifacts. To avoid these challenges, automated SPRi instruments have been introduced. Beusink, et al. [81] incorporated a hemispherical prism and an angle-controlled mirror to minimize the beam walk. However, the angle range was small, and it was not suitable for visualization of both liquids and gasses. Ruemmele, et al. [82] presented an inexpensive automated AM platform by mounting a sample/right-angle prism, a focusing lens, and a CCD camera on a single rotating stage. Although their system improved the precision and accelerated the angle scanning, it could not minimize the beam walk. Zhang, et al. [78] developed an automated SPRi instrument based on AM and IM. In their system, two motorized rotating stages create angular motions of the source light and CCD array. Like prior systems, this system could not eliminate the angle-dependent image artifact. In other research, Zhou, et al. [83] introduced an automated platform for SPRi with AM. This team used a rhombic structure with four connecting arms to convert the linear motion of a piezoceramic motor into the angular motion. Angular probing with high resolution, (i.e., 10^{-3} degrees), was possible with their setup. However, this AM platform could not resolve the issues arising from beam walk.

In this paper, we introduce a newly developed, high-precision angle-scanning SPRi platform that can minimize the angle-dependent image artifact. The developed automated SPRi instrument consists of two motorized linear stages and two motorized rotating stages. The light reflected on two angle-controlled mirrors allowed the incident angle to change from 40.0 to 80.0 degrees, while the linear stages corrected the beam walk by moving the CCD camera and the angle-controlled mirrors. This new SPRi instrument, capable of

imaging with AM and IM, was used for visualization of drop coalescence during dropwise condensation.

3.2 Automated SPRi Instrument

A schematic of our automated SPRi instrument is illustrated in Figure 3.1. A SugarCube^{TM} Ultra White LED illuminator (Nathaniel Group Inc., Vergennes, VT) is used as a light source. The optics, including an uncoated condenser lens (50 mm diameter, focal length 44 mm, PCX, Edmund Optics, Blackwood, NJ), two iris diaphragms (ID-0.5, Newport Optics, Irvine, CA), and an uncoated bi-convex lens (25.4 mm diameter, focal length 100 mm, KBX064, Newport Optics, Irvine, CA), are arrayed to produce a collimated beam with a diameter of ~ 20 mm. The light passes through a 550 nm hard coated bandpass filter with a full width-half maximum of 10 nm (Edmund Optics, Blackwood, NJ) and a rotatable polarizer (Thorlabs, Newton, NJ) to create a monochromic p-polarized light beam.

Mirror A is fixed at 135.0 degrees with respect to the positive direction of the x-axis to direct light toward the z-direction. Mirror C is mounted on a motorized rotating stage and can rotate clockwise. This mirror guides light to the prism. Mirror D is mounted on another motorized linear stage and can spin counter-clockwise. This mirror reflects the light beam vertically toward mirror B, which is fixed at 45.0 degrees with respect to the positive x-axis. Both motorized rotating stages are installed on a linear stage that moves along the z-axis. The integrated stages enable mirrors C and D to move in the z-axis and spin simultaneously. The SPR sensing system, consisting of a prism-metal-test medium, is fixed in space. A Photron APS-RS (PHOTRON USA Inc., San Diego, CA) camera is used to record the reflected light at high speed. The camera is mounted on a linear stage that can move along the x-axis. This automated SPRi instrument is controlled by a program written in the Arduino programming language and using an Arduino Mega 2560 Rev3 micro-controller. The same controller board triggers frame acquisition during SPRi with AM.

To minimize beam walk, the z motorized linear stage move according to a motion function. To find the motion function of the z motorized stage, the location of the z stage was adjusted at each incident angle such that the center of the light beam remains stationary at the center of a recorded image during angle-scanning. As the focus of an image at each incident angle affects the intensity of the recorded images and their corresponding reflectance, it is crucial to move the camera during angle-scanning to record focused images. The motion function of the camera's motorized linear stage was determined by adjusting the position of the camera to record focused and crisp images for each incident angle. Hence, the total light path-length of the reflected light from the gold surface to the camera is constant at any incident angles. Based on the calibration process, the motion functions of all motorized stages were determined and incorporated into the developed Arduino code.
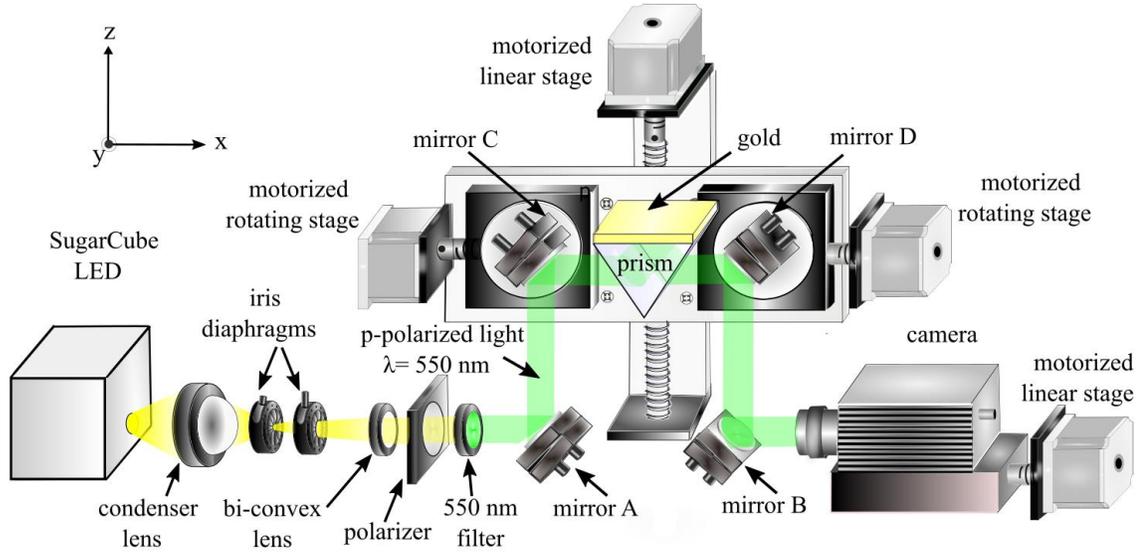
Figure 3.1 Schematic of the automated SPRi instrument.

3.3 Experimental Procedure

3.3.1 Application of the Automated SPRi Instrument for the Condensation/Evaporation Experiment

Figure 3.2(a) shows the schematic of the experimental setup. 2.5 nm of titanium as an adhesion layer and 50 nm of gold ($n = 0.4241 + 2.4721\ i$) was sputtered (Denton DV6 sputter deposition system) on a glass slide. We utilized atomic force microscopy (AFM) to conduct a roughness characterization of the gold substrate, Figure 3.2(b). The roughness characterization was performed on three gold surfaces (three different locations per sample). The roughness average (Ra) on the surface is 1.2 ± 0.3 nm and the root mean square of the average roughness (Rq) is 2.2 ± 0.8 nm. The static contact angle of the gold-coated glass is 79 ± 4 degrees. Before the experiment, the gold-coated glass slide and BK7 prism were cleaned using the standard cleaning protocol (10 minutes ultrasonic cleaning with isopropyl alcohol 99% (CAS 67-63-0, Pharmco Aaper), 10 minutes ultrasonic cleaning in Acetone (CAS 179124-4L-PB, Sigma Aldrich), and vigorous rinsing with DI water for 1 minute) to remove organic contamination on the sample. The ITO-coated glass was cleaned by sequentially rinsing in IPA, Acetone, and DI water. The gold-coated glass slide was placed on top of the right-angle BK7 prism (size 25.4 mm, $n = 1.5185$, 10BR08, Newport Optics, Irvine, CA) using a Norland Index Matching Liquid 150 (n =1.52, Norland, USA). SPRi with AM was performed to find the SPR minimum angle of air at 550 nm. To conduct the SPRi with IM, the incident angle was set at 44.8 degrees, which is 1.5 degrees below the SPR minimum angle of air. Selection of this experimental angle was based on its ability to achieve higher resolution in measurement of thin film on the substrate (see section 4.2). An ITO-coated glass slide was used as a heater and was placed approximately at 5 mm above the gold surface. A water column (diameter of ~ 2 mm and height of ~5 mm) was formed between the ITO-coated glass slide and the gold surface. The water column volume was maintained at 15 ± 5 µl during the experiment by manually

supplying water via a 500 µl threaded plunger syringe (Hamilton Company, Reno, NV). Two K-type thermocouples were placed on the gold substrate to monitor the temperature of the gold film. A third K-type thermocouple attached to the syringe needle was placed between the ITO-coated glass and the substrate to measure the air temperature. A sequence of background images was taken at 3,000 FPS from the substrate using the Photron APS-RS camera, prior to the onset of dropwise condensation.

Next, the water bridge was heated by connecting the ITO-coated glass to the DC power supply at 12.6 V and 2.1 A. During the heating process, water evaporates from the water-bridge and condensate forms on the gold substrate. Using ITO-coated glass as a heater was chosen over supplying heated water vapor on the substrate because ITO-coated glass confines dropwise condensation on the gold substrate and ensures no water film forms on the mirrors.

In our experiments, each CCD camera pixel covered 4 µm × 4 µm of the physical domain at a 550 nm wavelength. The field of view was 4 mm × 6 mm and the recording speed was 3,000 FPS. The temperature of the substrate was ~ 35 °C, and the temperature of the air was ~ 45 °C. The temperature of the air is higher than room temperature (24.5 °C), as the heater locally increased the temperature between the ITO-coated glass and the gold substrate. The relative humidity near the substrate where visualization takes place was estimated to be ~ 60 ± 4% using the August-Roche-Magnus formula. Measurement of the temperature of both the air and of the sample when condensation initiated enabled us to determine the relative humidity.
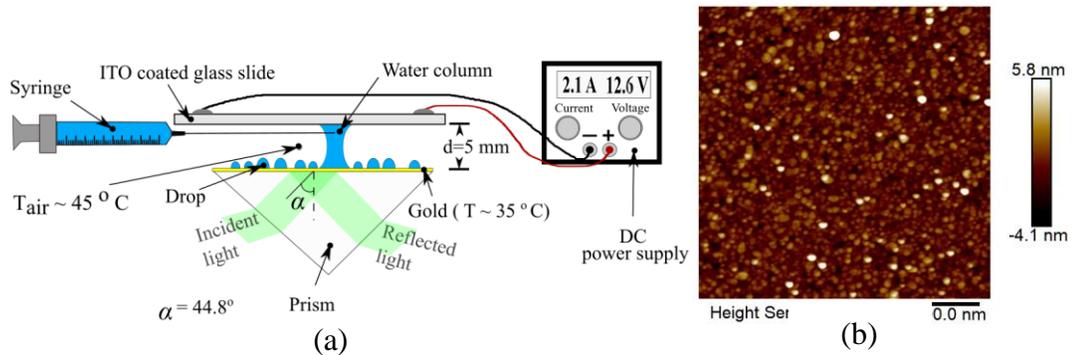
Figure 3.2 (a) Schematic of the condensation experiment and (b) gold substrate roughness measurement by AFM.

3.3.2 Image Processing Method

Two types of distortion exist in SPR images. First, the images are skewed along one of the axes of the imaging plane due to the oblique incident angle (α). In this work, the skewed images were modified by dividing the vertical axis of the image by $cos(\alpha)$. Figure 3.3(a) and (b) respectively show the raw image and the skewedness-corrected image of the condensation experiment. Because the object plane is not parallel with the image plane in SPRi, there are out-of-focus regions in the images. In the next step of image processing, the stack of background images was averaged over time and subtracted from the time-lapse image of the condensation experiment. This process alleviates the effects of non-

21

homogeneity in the gold layer or collimated light. The subtracted SPR image was converted to a color index image for easy visualization through a normalization process. The normalized image allows easy comparison between experimental results [84]. The colorful index image can help decipher details, such as a thin film measurement and material characterization, as compared with the analytical SPR results. To normalize the image and calculate the reflectance, a calibration factor is defined as $S = (I_{max} - I_{min})/(Ref_{max} - Ref_{min})$, where I_{max} and I_{min} represent maximum and minimum intensity from SPRi with AM. Ref_{max} and Ref_{min} indicate the theoretical maximum and minimum values of reflectance of air at 550 nm (Figure 3.1). Using a calibration factor, we can convert the pixel intensity value to the unit of reflectivity (0~1). A detailed description of the reflectance calculation and image processing method used in this work can be found in our recent paper [2]. The normalized image with the reflectance unit is shown in Figure 3.3(c). The yellow color with the reflectance of 0.594 represents the bulk liquid on the gold substrate; the blue color with the index of 0.347 shows the presence of air/water vapor on the substrate. Our SPRi instrument cannot differentiate the gasses (the difference in refractive index of gasses in ambient conditions is on the order of 1e-4, which is beyond the capability of our SPRi instrument to measure refractive index); thus, we can be sure that gas (air/ water vapor) exists on the surface. Due to high-speed imaging (low light), the noise level is high in the image. Therefore, the reflectance at each pixel of the background image fluctuated around 0.347.
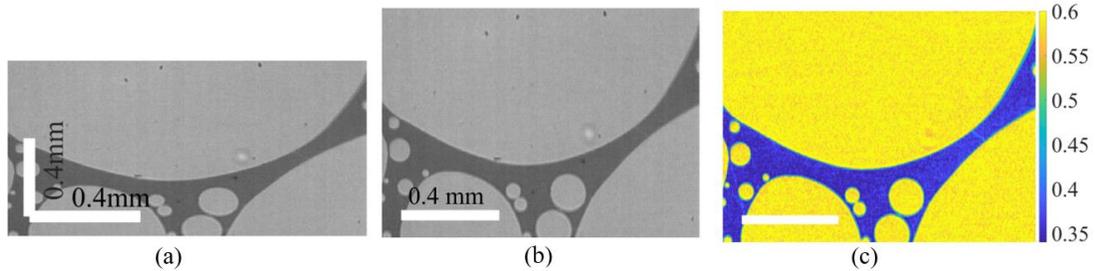
Figure 3.3 (a) Raw image, (b) a skewedness-corrected SPR image derived by dividing the vertical axis of the image plane by cos(α), and (c) normalized SPR images with the reflectance unit

3.3.3 Noise Analysis in High-speed SPRi

One of the main goals of this article is to show the feasibility of measuring sub-nanometer film at high-speed temporal resolution. In order to report measured values of thickness with high confidence, the error associated with the measurement is required to be some fraction of the thickness being measured. In measuring techniques based on imaging, noise causes imprecision in measurement of pixel intensity values. This section details the noise analysis method used in high-speed SPRi. The noise analysis result is used to find the error of the thickness measurement.

Noise in the signal has a stochastic nature; in addition, it adds a random unwanted fluctuation to the signal. Random fluctuation in the signal is difficult to identify as the measurement of a signal at one time, and one location, does not provide information about

the next or previous frame. Noise in the SPRi is produced by factors such as instability in the illumination light, nonhomogeneous light, vibration, shot noise, sensor temperature, lens distortion, and digitization hardware. The systematic noise, like the noise created due to nonhomogeneous light, is reduced during image processing by subtracting the background image from the condensation image. The remaining noise in the signal can be characterized in two ways – Gaussian noise and signal-dependent noise. The Gaussian noise is independent of signal intensity; its value at each pixel is calculated by an independent draw from a Gaussian probability distribution. The signal-dependent noise, including the shot noise (i.e., fluctuations of the number of photons detected at a given exposure level), the fluctuation in light, and the vibration, follows a Poisson distribution. In practice, signal-dependent noise has the lower bound on the uncertainty of measuring light; further, noise in the imaging can be modeled using a Gaussian distribution [85]. A simple technique to reduce the Gaussian noise is to calculate the average value of the neighbors of a pixel. In this method, each pixel output is the mean value of its kernel window.
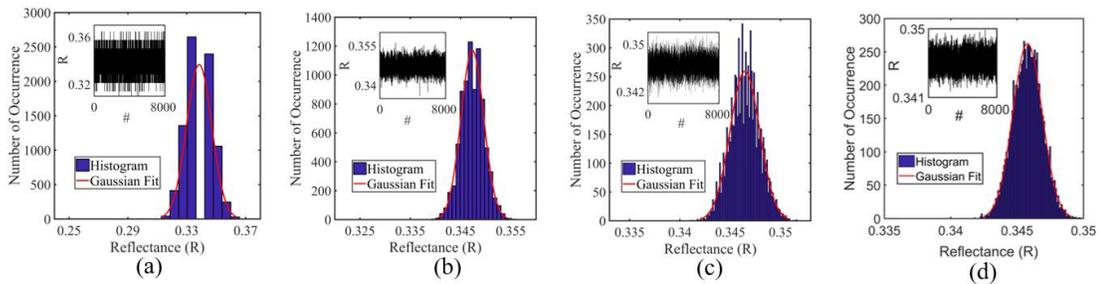
Figure 3.4 Analysis of SPR image noise – at an experimental angle of 44.8 degrees, a temporal resolution of 3,000 FPS, and a spatial resolution of 4 μm– by averaging the reflectance signals over kernel windows of (a) 1×1 pixels, (b) 5×5 pixels, (c) 9×9 pixels, and (d) 17×17 pixels; # stands for frame number.

`

Table 3.1 Signal-to-noise ratio and coefficient of variation of the reflectance signal at different kernel windows.

Kernel windows	Signal-to-noise ratio	Coefficient of variation
1×1	39 ± 4	0.026 ± 0.003
3×3	104 ± 12	0.0093 ± 0.0008
5×5	163 ± 6	0.0057 ± 0.0007
9×9	228 ± 23	0.0044 ± 0.0004
17×17	307 ± 23	0.0032 ± 0.0002

Image noise was analyzed by picking a pixel randomly and calculating the mean values of the signal over the pixel neighborhoods of 1×1, 3×3, 5×5, 9×9, and 17×17 at each frame. The same procedure was repeated at ten random locations of the image. Figure 3.4

demonstrates the reflectance of the pixel at kernel windows of 1×1, 5×5, 9×9 and 17×17 pixels. At each kernel window, two plots are illustrated: 1) signal (reflectance) fluctuation during the time-lapse imaging, and 2) histogram of the signal. The total number of time-lapse images is 8,000 and each frame takes 0.33 ms. The histogram at all the kernel windows can be fitted with a Gaussian distribution. The result verifies the assumption that behavior of noise in high-speed SPRi can be described with a Gaussian distribution. The signal-to-noise ratio and the coefficient of variation are calculated from the noise analysis result (see Table 3.1). These values are used to quantitatively estimate the probability of noise during high-speed imaging of condensation. Signal-to-noise ratio – the mean of the signal over its standard deviation – increases from 39 ± 4 to 307 ± 23 when the kernel window changes from 1×1 to 17×17. The higher signal-to-noise ratio implies less noise in the reflectance measurement. Coefficient variation – the ratio of standard deviation over the mean value of a signal – represents the dispersion of a signal around the mean value. Using a kernel window of 5×5, the probability of noise at each pixel is reduced to ± 0.0057 of the signal value.

We employed an averaging filter with pixel neighboring of 5×5 to the normalized images. This size of filter confines the noise at each pixel to ± 0.0057 of the signal values, while not sacrificing details of the image due to a blurring effect.

3.3.4 Uncertainty Evaluation for SPR Reflectance

Uncertainty analysis was conducted based on single point detection estimation [37, 86]. The resulting reflectance can be calculated from $R_{SPR} = f(\varepsilon_1, \varepsilon_2, \varepsilon_3, \varepsilon_4, d_2, \lambda_i, \alpha, d_3)$ where subscript 1, 2, 3, and 4 refer to the BK7 prism, gold, water, and air. The uncertainty of reflectance can be evaluated as:

$$\omega_{R_{SPR}} = \pm \left[\begin{array}{l} \left(\frac{\partial R_{SPR}}{\partial \varepsilon_1}\omega_{\varepsilon_1}\right)^2 + \left(\frac{\partial R_{SPR}}{\partial \varepsilon_2}\omega_{\varepsilon_2}\right)^2 + \left(\frac{\partial R_{SPR}}{\partial \varepsilon_3}\omega_{\varepsilon_3}\right)^2 + \left(\frac{\partial R_{SPR}}{\partial \varepsilon_4}\omega_{\varepsilon_4}\right)^2 \\ + \left(\frac{\partial R_{SPR}}{\partial d_2}\omega_{d_2}\right)^2 + \left(\frac{\partial R_{SPR}}{\partial \lambda}\omega_{\lambda}\right)^2 + \left(\frac{\partial R_{SPR}}{\partial \alpha}\omega_{\alpha}\right)^2 + \left(\frac{\partial R_{SPR}}{\partial d_3}\omega_{d_3}\right)^2 \end{array} \right]^{1/2} \quad (3.1)$$

where the elementary uncertainties are estimated as $\omega_{\varepsilon_1} = 0.01\% \times \varepsilon_1$, $\omega_{\varepsilon_2} = 0.1\% \times \varepsilon_2$, $\omega_{\varepsilon_3} = 0.01\% \times \varepsilon_3$, $\omega_{\varepsilon_4} = 0.01\% \times \varepsilon_4$, $\omega_{d_2} = 0.1\% \times d_2$, $\omega_{\lambda} = \pm 5$ nm, $\omega_{\alpha} = 0.2$ degrees (beam divergence), and $\omega_{d_3} = \pm 0.125$ nm (uncertainty of a monolayer thickness measurement). The uncertainties of the prism, water, and air are assumed to be negligible because of their small variation of 0.01 %. The uncertainty of reflectance at 0 nm and monolayer thickness of thin water film is close to ± 0.07. All the variables are taken at the test condition ($\varepsilon_2 = -5.931 + 2.097\,i$, $d_2 = 50$ nm, $\lambda = 550$ nm, and $\alpha = 44.8$ degrees). The effect of beam divergence has the maximum weight on the estimated uncertainty for the reflectance measurement when considering only the reflectivity. Under this restriction, the estimated reflectance uncertainty is larger than the monolayer thickness measurement. However, additional factors need to be considered when discussing the uncertainty in the thickness measurement. First, the intensity value of the background image is subtracted from the pixel intensity value of the time-lapse image of condensation. This process reduces the effect of beam divergence on the reflectance

uncertainty. For example, when the thickness of the water film is zero on the gold surface, the reflectance ($\lambda = 550$ nm and $\alpha = 44.8$ degrees) of the pixel is 0.347 ± 0.03. The error in measured reflectance is less than estimated uncertainty using equation (1). Second, we are using the concept of pixel neighboring to reduce the error of the reflectance measurement at a single pixel when measuring the reflectance of the thin film and computing the corresponding film thickness. Third, the field of view in our work is located approximately at the center of the incident beam on the BK7-gold interface. The size of the field of view is 4 mm × 6 mm which is only ~ 7 % of the cross-sectional area of the beam. As a result, the net effect of beam divergence on the reflectance uncertainty is much less than the estimated value, based on the total prism area.

3.4 Results and Discussion

This section first lists the advantages of automated SPRi in high-speed visualization of phase change phenomena. The discussion includes advancement of SPRi with AM, and ambient-temperature-independent reflectance measurement. Then, the results of visualization of dropwise condensation are discussed and compared with theories of the dropwise condensation mechanism.

3.4.1 Advantages of Automated SPRi in Visualization of Phase Change Phenomena

3.4.1.1 Advancement of SPRi with AM

One critical challenge in angular SPRi is the fine adjustment of incident light, optical arrays, the prism, and the CCD camera at each incident angle. Operator skill during angle-scanning can cause large uncertainty in SPRi with AM. On the other hand, the process of angular tuning of the setup requires meticulous care and is time-consuming. Our newly developed automated SPRi platform resolved these issues associated with conventional angular SPRi. The user can define the angular increment for the scanning from 10^{-3} to 1.0 degrees easily through the controlling program. Each increment takes about 3s. Depending on the desired precision and the angle range, the time required for angular scanning is different. Figure 3.1 represents the theoretical and experimental reflectance curve of air at 550 nm. Details about the approach used in this work to find the theoretical reflectance can be found in Yamamoto [87]. The error bar shows the experimental results for 5 different sets of experiments. Each experiment took approximately 1 minute to complete. The SPR signal behavior perfectly matches with the theoretical result around the maximum and minimum points of the curve. The deviation from the theoretical result increases between these two probing angles or at an angle larger than the SPR minimum. The maximum discrepancy between the experimental and the theoretical results is at the incident angles smaller than the internal reflection angle (41.2 degrees). The experimental reflectance curve is in closer agreement with the theoretical reflectance curve when a smaller angle step is selected for the SPRi with AM.

As Figure 3.1 shows, small changes in the incident angle can cause a significant change in the reflectance. Hence, knowing the exact position of the incident angle is crucial for analysis related to SPRi with IM. Having motorized rotating mirrors enabled us to adjust

the incident angle by minimizing human error that may occur when using a manual SPRi instrument. Moreover, once the incident angle was fixed, we double-checked the position by experimentally measuring the reflectance of air and water (bulk) at the fixed angle and wavelength. The reflectance was measured by dividing the averaged intensity of recorded images in light in the p-polarized mode over the averaged intensity of recorded image in the s-polarized mode. The s-polarized image was recorded by changing the rotatable polarizer 90 degrees.
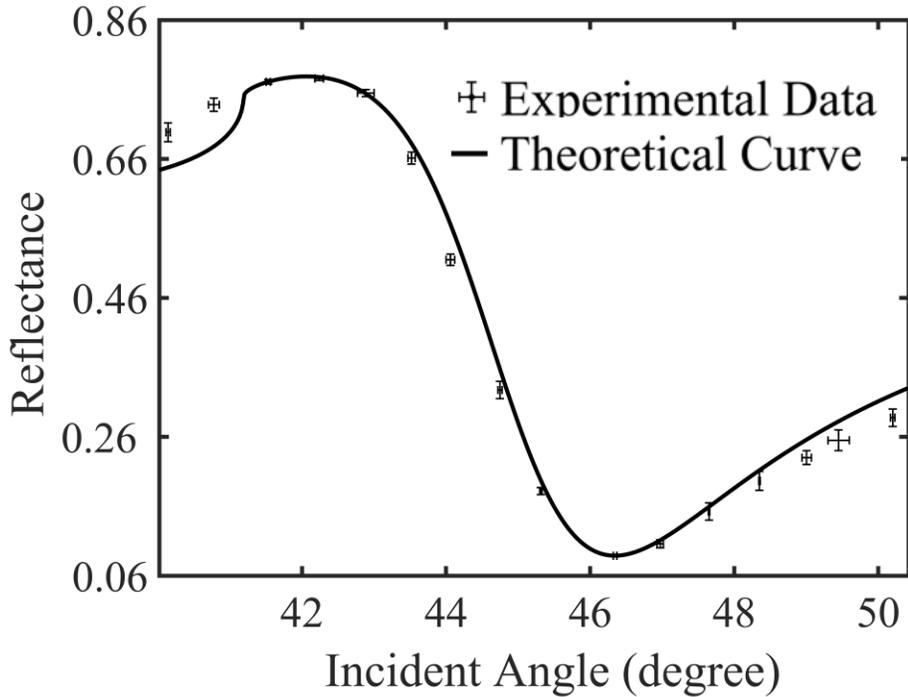
Figure 3.1 Theoretical and experimental SPR reflectance comparison of air at 550 nm (the error bar represents the deviation in the measurement based on 5 data sets).

3.4.1.2 Ambient-temperature-independent Reflectance Measurement

Condensation experiments are usually performed using a Peltier stage, which induces a fixed temperature on the surface. However, our experiments were not conducted using a Peltier stage, and the temperature of the gold substrate was recorded during the experiment. SPR reflectance can be affected by temperature changes [88, 89]. Therefore, it was imperative to consider the temperature-dependent behavior of SPR when we were analyzing the recorded images. Theoretical modeling and experimental investigation were implemented to evaluate the effect of temperature. SPR reflectance depends on the optical properties of the BK7 prism, the gold, and the test medium (air or water). It has been shown that the refractive index of the BK7 prism only changes 0.0002 when temperature changes from 25 °C to 125 °C [90]. Thus, in this work, we can neglect the effect of the BK7 prism as the temperature on the gold changed only from 25 °C to 35 °C. According to the Lorenz-Drude-temperature model [91], temperature variation can affect the optical properties of

gold by changing the plasmon frequency and the electron collision rate. This model was used to simulate the effect of temperature on the gold's optical properties.

The air and water refractive indices decrease with an increase in temperature. The sensitivity of our SPRi instrument in measuring the refractive index was less than the refractive index changes of the air. Therefore, we can consider the temperature-independent behavior for air. The change of the refractive index of water as a function of temperature was modeled using the empirical relationship [92]:

$$n(\lambda,T) = A(T) + \frac{B(T)}{\lambda^2} + \frac{C(T)}{\lambda^4} + \frac{D(T)}{\lambda^6}$$

$$A(T) = 1.3208 - 1.2325 \cdot 10^{-5}T - 1.8674 \cdot 10^{-6}T^2 + 5.0233 \cdot 10^{-9}T^3$$

$$B(T) = 5208.2413 - 0.5179T - 2.284 \cdot 10^{-2}T^2 + 6.9608 \cdot 10^{-5}T^3 \qquad (3.2)$$

$$C(T) = -2.5551 \cdot 10^8 - 18341.336T - 917.2319T^2 + 2.7729T^3$$

$$D(T) = 9.3495 + 1.7855 \cdot 10^{-3}T + 3.6733 \cdot 10^{-5}T^2 - 1.2932 \cdot 10^{-7}T^3$$

Figure 3.2(a) shows the SPR reflectance curve for air and water at 550 nm when the temperature changes from 25 °C to 75 °C. The model predicted that the SPR curve of air would shift slightly to the right with an increase in temperature. At the SPR minimum angle of air at 550 nm, the air reflectance changes less than 1% with a 50 °C increase in temperature. Simulation of the water reflectance curve at 550 nm indicated that the water reflectance curve drastically changes with rises in temperature; however, the reflectance variation is less than 1% when the incident angle is between 30.0 to 55.0 degrees − we performed the condensation visualization at 44.8 degrees. Also, we experimentally depicted the SPR signal behavior with the temperature changes at a probing angle of 46.3 degrees and a wavelength of 550 nm (see Figure 3.2(b)). The reflectance of the SPR signal was measured using the same method discussed in the image processing section. The temperature on the x-axis represents the temperature of the gold substrate. The air temperature is ~ 20 °C more than the substrate and the water temperature is ~ 10 °C more than the substrate temperature. The reflectance changes represent the accumulative dependence of the SPR sensor, including the BK7 prism, the gold substrate, and the index matching liquid. The result indicates the reflectance variation is less than 1% when the gold temperature varies from 25 °C to 70 °C, the incident angle is 46.3 degrees, and the wavelength is 550 nm. Both experimental and theoretical results show the change in reflectance is less than 1%.

In summary, the nearly temperature-independent behavior of the SPR signal close to the SPR minimum angle of air allows visualization of the condensation/evaporation process without a thermally controlled test chamber between 25 °C to 70 °C. This means by carefully selecting the probing angle, the phase change phenomena visualization experiment can be carried out in ambient conditions. This significantly reduces the costs of the experiment. In the dropwise condensation experiment (see Figure 3.2), the temperature of the air is ~ 45 °C and the temperature of the gold is ~ 35 °C; this is in the range (25 °C to 70 °C) of the temperature-independent behavior that is shown. It is possible to use the SPRi technique in the case of higher-temperature ambient conditions (such as

condensation of steam at 100 °C) if the incident angle and wavelength of light are chosen wisely. However, surface degradation needs to be studied when working with steam at 100 °C. For example, volatile organic compounds may desorb at higher temperatures and affect the wettability of the surface as well as the water molecules' adsorption kinetics.

(a)   (b)
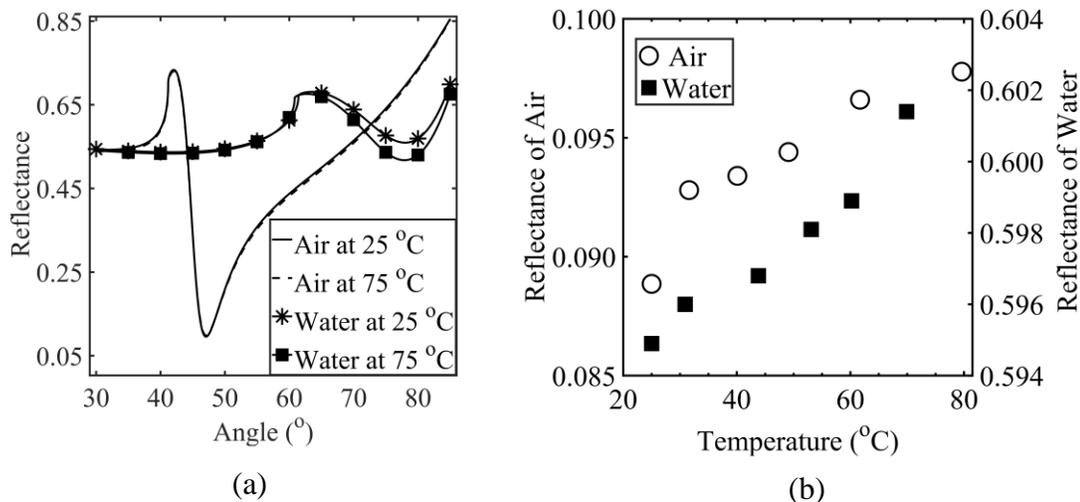
Figure 3.2 Temperature-dependent behaviors of the SPR signals in air and water environments: (a) the theoretical model shows the change in reflectance at a probing angle of 46.3 degrees and wavelength of 550 nm is less than 1% and (b) the experimental data indicates that at a fixed angle of 46.3 degrees and wavelength of 550 nm, the changes in reflectance are less than 1 % for both air and water when the temperature of the gold substrate changes from 25 °C to 70 °C (temperature of air and water are respectively ~ 20 °C and ~ 10 °C higher than the substrate).

3.4.2 Dropwise Condensation

The dropwise condensation process begins by nucleation of droplets on the substrate and subsequent growth of these droplets without significant interactions with neighboring droplets. In the next stage of dropwise condensation, two or more adjacent droplets coalesce and produce a larger composite droplet. Droplet motion due to coalescence exposes part of the substrate to the ambient air; then, the nucleation process is repeated at the exposed area. This condensation cycle continues on the substrate. In this section, we shed light on the dropwise condensation mechanism by studying the fluid-solid interface during coalescence phenomena.

It has been shown that volatile organic compounds can absorb rapidly on the surface and change wettability of the metal substrates [93-96]. Gold that is intrinsically hydrophilic can support dropwise condensation when it is in the ambient atmosphere [23]. In this work, since low condensation rates were implemented to conduct the experiment, condensation on the gold-coated glass remained dropwise during the experiment. As the initial goal of our experiment did not include recording the droplet growth rate and condensation rate, we can only provide an estimate. The changes of wetted area by the water column on the gold surface can be attributed to the evaporation (evaporation rate is approximately 0.01 µl/s).

28

Using RH = (condensation rate / evaporation rate) × 100 where RH is ~ 60%, the estimated condensation rate is ~ 0.006 µl/s. Knowing the surface coverage of condensates (approximately 7 mm2), the heat flux at the surface can be estimated (q″ = (condensation rate / surface coverage) × density × enthalpy of evaporation) as 0.2 W/cm2. The order of magnitude of the droplet growth rate is estimated to be 1 µm/s in diameter. The droplet growth rate and heat transfer rate were quite low mainly due to the presence of non-condensable gases [15, 97]. Figure 3.3 illustrates the evolution of coalescence on a gold substrate. Filter averaging of 5 × 5 was applied on the normalized images to reduce the image noise. The initial status of the drop before coalescence is depicted in Figure 3.3(a). The yellow color shows the droplet, and the blue color represents the area between droplets (from here on it is called an inactive area). During the coalescence, the involved droplets move on the substrate, which exposes part of the surface to the water vapor in the ambient air. From here on, the exposed area after the coalescence is called a preoccupied area. Figure 3.3(b) illustrates the preoccupied area after 9 ms from the start of coalescence. After the coalescence event, new small droplets form on the preoccupied area, as shown in Figure 3.3(c).

(a)　　　　　　　　　　(b)　　　　　　　　　　(c)
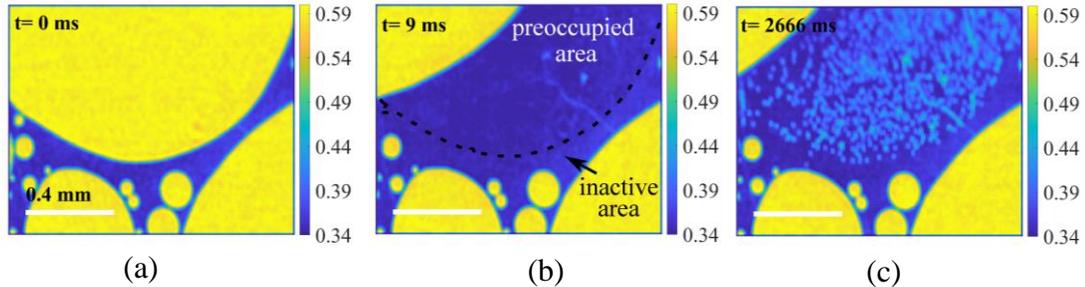
Figure 3.3 Coalescence evolution: (a) initial positions of droplets before coalescence; the yellow color represents water and the blue color signifies air, (b) an exposed part of the substrate after the droplet motion during coalescence – the exposed area (preoccupied area) is distinct with a slightly different color index, as compared to the ambient (inactive area) result, and (c) nucleation of new droplets in the preoccupied area only

It can be observed from Figure 3.3(b) that the preoccupied area has a slightly different color from the inactive area. For easy visualization, the contrast of this image has been enhanced by changing the range of the color map (see Figure 3.4(a)). To compare the reflectance of the inactive and preoccupied areas, the averaged reflectance of each site was calculated. The preoccupied area with 27500 pixels has the averaged reflectance of 0.34582 ± 1.2 E-5, which is very close to the reflectance of a gold-air interface. The standard error (i.e., ± 1.2 E-5) is measured by dividing the standard deviation of noise at each pixel (i.e., 0.0057 of the signal value) by the root mean square of the number of observations, 27500. The averaged reflectance of the inactive area with 15000 pixels is 0.35401 ± 1.6 E-5. The difference of reflectance between the preoccupied and the inactive areas is 0.00819, which is more significant than the standard errors of the measurement. The difference in the reflectance values at the two sites indicates there exists a material difference between the preoccupied area and the inactive area. SPR reflectance at the fixed angle and wavelength depends on the refractive indices and the thickness of the test media involved. As the

refractive index of air and water is constant over the entire study area, the difference of reflectance values can only be attributed to the changes in the thickness of the water film.

Figure 3.4(b) depicts the theoretical SPR curve at 550 nm for a 4-layer medium (BK7 prism, gold, thin water film, and air) with different thicknesses of water film. It can be seen in the figure that the sensitivity in measuring thin film is higher when SPRi with IM is performed at 1.0~3.0 degrees, far from the SPR minimum angle of air; that is the reason that 44.8 degrees was selected as the experimental angle for SPRi with IM. At this angle, a monolayer thickness of water film (0.275 nm) yields a 0.01150 increase in the SPR reflectance value (see Figure 3.4(c)). As the reflectance of the preoccupied area is very close to the reflectance of the gold-air interface, it can be concluded that only air exists on the gold surface, i.e., the preoccupied area is a dry zone. However, the reflectance of the inactive area is 0.00819 larger than the reflectance of the gold-air interface and the 0.00819 of reflectance unit indicates the presence of a molecularly adsorbed water film (not high-concentration water vapor nor adsorbed volatile organic compounds). The surface coverage of this adsorbed monolayer of water in our experiment is 0.71 (m^2/m^2) (see section4.4.2.1). It should be mentioned that it is likely that droplets constantly evaporate on the surface due to the high temperature of the substrate (~ 35 °C); this may cause a high concentration of water vapor around the droplets. However, the automated SPRi instrument cannot differentiate the difference between gasses, i.e., the sensitivity of the SPRi instrument in measuring the refractive index is less than the change of refractive indices from air to high-concentration water vapor.

The aforementioned standard cleaning protocol using isopropyl, acetone and DI water cannot remove the adsorbed volatile organic compounds from the surface [95, 96, 98, 99]. It was likely that adsorbed organic compounds were present on the surface even prior to the visualization experiment. Moreover, the preoccupied area that emerges after the coalescence is dry, i.e., it does not have the adsorbed water thin film. It has been reported that DI water cannot remove adsorbed organic compounds on the surface (Saga and Hattori 2005). This means that if an organic adsorbed film exists on the surface, it cannot be removed by the droplet. As the reflectance measurement was conducted by subtracting the pixel value of the background images from condensation mages, the net effect of adsorbed volatile organic compounds on the reflectance would be zero or negligible. Therefore, the changes in reflectance cannot be attributed to the adsorption of volatile organic compounds on the surface.

The nucleation of droplets at the preoccupied area can be explained with the new experimental results. The adsorption of vapor molecules on the surface minimizes the surface energy of the substrate. As the preoccupied area is dry, it has higher surface energy compared to the inactive area between the droplets. The preoccupied area with high surface energy serves as a favorable site for water vapor to condense and nucleate on the substrate, as shown in Figure 3.3(c). We cannot comment on the evolution of the dry zone between 9 ms and the time when nucleation starts; this is because the spatial resolution (4 µm) is larger than the size of the first nucleus. In our future work, we will answer to the question of whether an adsorbed film forms on the dry zone, followed by nucleation or whether the vice-versa scenario occurs.
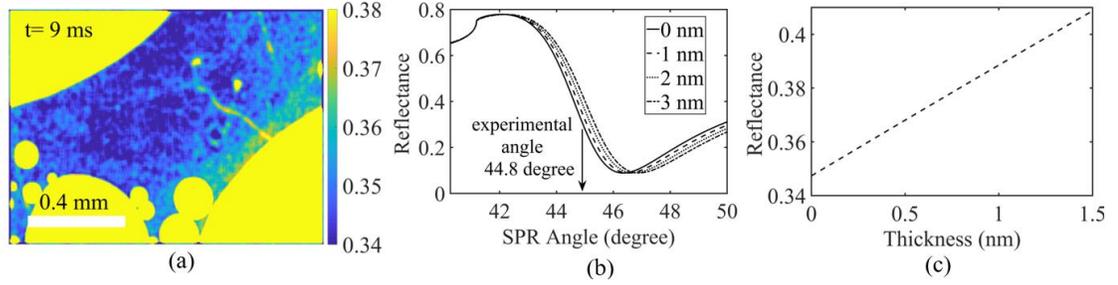
Figure 3.4 (a) Reflectance of the inactive area is 0.00819 larger than preoccupied area with reflectance of 0.34582, (b) theoretical SPR curve for the 4-layer medium (BK7 prism, gold layer, thin water film, and air) with different sizes of water film at 550 nm, and (c) the change of reflectance with the increase in the size of the water film at 44.8 degrees; the reflectance of the preoccupied are represents the dry area on the substrate and the reflectance of the inactive area shows the existence of a monolayer film between droplets.

3.4.2.1 Mechanism of Dropwise Condensation

There is no united understanding of dropwise condensation phenomena because of the complexity of the physics involved. The mechanism of dropwise condensation has been under debate for the past 90 years [69]. Two main theories have emerged; both theories have been supported with experimental results [23, 25]. However, the experimental methods used in these studies were not able to measure sub-nanometer film thicknesses at high speeds (>1,000 FPS) in ambient conditions. ***To the knowledge of the authors, this is the first time that the coexistence of an adsorbed film between a droplet and the dry zone at the preoccupied area during dropwise condensation has been experimentally reported.***

Although the film rupture theory can explain the existence of a thin film between the droplets, it is unable to explain the existence of a dry zone at the preoccupied areas. Thus, the results of this study undermine the validity of film rupture theory. Our results suggest that either nucleation theory or a combination of both film rupture and nucleation theory can explain dropwise condensation on a solid substrate.

The average thickness of the absorbed layer between droplets presented here can be explained with the theoretical approach that Umur and Griffith [23] used in their work. According to the adsorption theory, molecules in the gas can adhere to the solid surface. The fraction of a surface covered by adsorbed molecules is called surface coverage. Langmuir theory [100] explains that striking molecules on the surface can adsorb them to the surface; subsequently, they evaporate from the surface. Under an equilibrium condition, the rate of adsorption is equal to the rate of evaporation. The Langmuir isothermal model assumes the maximum surface coverage of the adsorbed molecule is one monolayer. The rate of adsorption on a surface and evaporation from the surface, respectively, can be expressed as:

$$r_a = k_a \frac{P}{\sqrt{2\pi m K_B T}} \qquad (3.3)$$

$$r_d = k_0 \Lambda e^{\frac{-w}{R(T+273.15)}} \tag{3.4}$$

To find the surface coverage during dropwise condensation, consider a solid substrate that has interface with both vapor and liquid under an equilibrium condition (T and P are constant). For this system, we can write at the solid-vapor interface (subscript s) and liquid-vapor interface (subscript l), respectively:

$$k_{as} \frac{P}{\sqrt{2\pi m K_B (T+273.15)}} = k_0 \Lambda_s e^{\frac{-w_s}{R(T+273.15)}} \tag{3.5}$$

$$k_{al} \frac{P}{\sqrt{2\pi m K_B (T+273.15)}} = k_0 \Lambda_l e^{\frac{-w_l}{R(T+273.15)}} \tag{3.6}$$

For the liquid interface, Λ_l is one. By dividing equation (3.5) by equation (3.6), the Λ_s can be expressed as:

$$\Lambda_s = \frac{k_{as}}{k_{al}} e^{\frac{w_l}{R(T+273.15)}(\frac{w_s}{w_l}-1)} \tag{3.7}$$

The values for k_{as} and k_{al} are close to unity; therefore, their ratio can be considered to be one. It can be shown that the work of adhesion between the solid-liquid interface to the work of cohesion between the liquid-liquid interface is [101];

$$\frac{w_s}{w_l} \approx \frac{1}{2}(1 + \cos \xi) \tag{3.8}$$

For the case of dropwise condensation where ξ is larger than zero, the w_s/w_l is smaller than one. Using the properties of water at the pressure of 1 bar and temperature of 35 ºC and considering molar latent heat of 43.56 kJ/mol instead of w_l, one obtains $\Lambda_s < 1$ (m^2/m^2). The average thickness of the surface is proportional to the surface coverage. Surface coverage in our experiment can be obtained to be 0.71 (m^2/m^2). Our measurement shows the thickness of the adsorbed layer is not greater than a monolayer in majority of the inactive area. However, based on our visualization, there are some limited locations on the inactive area, such as the area between two large droplets (see Figure 3.3(a)) that have a local thickness of more than one monolayer. We are not certain whether these areas have adsorbed film more than a monolayer or if they are covered with micro/nano droplets less than the spatial resolution of our imaging (4 μm). In either case, the effect of these areas is neglected in the heat transfer models developed based on the nucleation theory of dropwise condensation [102]. It is possible to further improve the spatial resolution of SPRi [86]. In our future studies, we will enhance the spatial resolution (550 nm) of the SPRi instrument to study these high-density areas on the substrate, and interaction of water molecules in the adsorbed layer with neighboring droplets. Moreover, the mechanism of initial drop formation at the onset of condensation will be studied to enable a full view of the dropwise condensation mechanism on the solid substrate.

3.5 Conclusion

The current study developed an automated, angle-scanning SPRi instrument by integrating linear and rotating motorized stages. This instrument improves the conventional SPRi that uses the AM technique by enhancing the resolution of angle probing, increasing the speed of angle scanning, and minimizing the angle-dependent image artifact. This automated instrument can perform angle scanning at a range of 40.0 to 80.0 degrees, which is suitable for sensing a variety of organic dielectrics, including air and water. The angular resolution can easily be adjusted from 10^{-3} to 1.0 degrees, depending on the precision required for an experiment. The instrument has a large field of view, which is perfect for studies related to fluid dynamics applications. The SPRi instrument, combined with high-speed imaging, introduces a new tool for real-time imaging of phase change phenomena, such as drop coalescence, condensation, and evaporation. Our newly developed, automated SPRi instrument successfully recorded the evolution of drop coalescence at 3,000 FPS and a spatial resolution of 4 µm. This SPRi instrument will be able to achieve higher spatial and temporal resolutions when a stronger illumination system and a larger NA objective lens are implemented for the imaging. We numerically and theoretically demonstrated that the SPR signal dependence on temperature close to the SPR minimum angle of air is less than 1% when the temperature changes from 25 °C to 70 °C. This means that there is no need for a thermally controlled test chamber or a Peltier stage for visualization of phase change phenomena. The probability of noise in the imaging was studied and used to measure the standard error of the thin film measurement. Our observation of dropwise condensation reveals 1) the presence of a thin film with thickness of one monolayer, and 2) surface coverage of 0.71 m^2/m^2 by the thin film in the area between the droplets. When the coalescence happens, the droplet motion wipes part of the substrate and leaves a dry area behind. The dry area serves as a new site for drop nucleation. Our high-speed SPRi instrument for thickness measurement provides experimental data that shows – for the first time – the coexistence of a dry area and adsorbed film on the substrate during dropwise condensation. The results of this work cast doubt on film rupture theory as the dropwise condensation mechanism. In future work, we will enhance the sensitivity and spatial resolution of our SPRi instrument to have a more in-depth study on the nucleation phase of dropwise condensation.

4 The Effect of Adsorbed Volatile Organic Compounds on an Ultrathin Water Film Measurement

The physics of dropwise condensation has been under study for more than nine decades [1,2]. However, despite a significant body of prior work, there is still not a united theory behind the physics of dropwise condensation [3]. The main differences between the theories are (I) whether a thin film forms on a surface and ruptures to form droplets or the droplets nucleate heterogeneously on a surface, (II) whether a thin film exists between the droplets during the dropwise condensation, and (III) whether the thin film between the droplets contributes to the overall heat transfer from a surface [4]. To clarify these ambiguities about the physics of dropwise condensation, it is required to atomistically probe the solid–vapor interface during phase-change to evaluate the existence and structure of the thin film and initial nuclei that develop during condensation. In this regard, we have recently shown for the first time the existence of a monolayer film of water between droplets during the dropwise condensation on a smooth gold surface; this work was enabled by surface plasmon resonance imaging (SPRi) at 3000 frames per second (FPS) [5,6]. In our prior manuscripts, we discussed the development of the experimental apparatus and the uncertainty/error of the imaging. Another type of error that can affect water thin film identification and measurement is related to surface properties. As properties of a surface can affect the heterogeneous nucleation, it is necessary to study surface heterogeneity and subsequent influence on thin film measurement results. Surface roughness [7–9] and surface contamination [10–12] are among the reasons for surface heterogeneity.

Surface contamination is a critical problem in the thickness measurement, specifically ultra-thin film thickness ($1 < $ nm) [13]. Inevitable contamination, such as adsorbed volatile organic compounds (VOCs) on a surface, interfere with measuring the thickness of a thin film by changing the refractive index and thickness of the thin film [14]. VOCs are airborne and can manifest in the form of chlorinated hydrocarbons, aromatic hydrocarbons, mono- and polyalcohols, and ketones [15]. Storing samples to minimize the accumulation of contaminants and surface treatment to minimize the effect of VOCs on a surface are the routine preprocessing steps before measuring a thin film using SPRi [16]. Although these steps minimize the amount of unwanted adsorbed VOCs on a surface before an experiment, the adsorption of VOCs on a surface during an experiment is inevitable. In particular, the effect of adsorbed VOCs on a measuring signal can be considerable when the measurement takes in the ambient atmosphere and runs for a long time–such as in the case of identifying a thin film that may exist between droplets during the dropwise condensation on a smooth surface.

In this work, two surface-treatment procedures were studied for removing contamination and particles from the gold surface. The effects of these two cleaning procedures on the surface uniformity, surface wettability, surface chemistry, and adsorption of VOCs were studied using atomic force microscopy (AFM) [17], optical microscopy [18], X-ray photoelectron spectroscope meter (XPS) [19,20], and SPRi [21]. Through this research, the cleaning procedure that has the minimum effects on ultrathin film measurement using SPRi was identified, and the error associated with the adsorption of VOCs during thickness measurement of an ultrathin water film was characterized.

4.1 Materials and Methods

4.1.1 Sample Fabrication

Plain glass slides (75 mm × 25 mm × 1 mm, catalog number 48300-026, VMR International, Randor, PA, USA) were immersed in a piranha solution (a mixture of H_2SO_4 and H_2O_2) for 20 min to remove residues of organic contaminations on the glass surface, followed by thoroughly rinsing with water and drying with nitrogen prior to the gold deposition procedure. Then, 2.5 nm of titanium as an adhesion layer and 50 nm of gold (*n = 0.4241 + 2.4721 i)* were deposited on the glass slides using a Denton DV6 sputter deposition system. Samples were left in ambient conditions (an average relative humidity of 33% and an average temperature of 28 °C) for three months before using them for the surface characterization experiments. The period of three months provided enough exposure time for the adsorption of VOCs on the surface [11,12]. Gold-coated samples were cut into pieces and cleaned using a standard cleaning protocol (SCP) before the surface characterization experiments using the following procedure—10-min ultrasonic cleaning in acetone (CAS 179124-4L-PB, Sigma Aldrich, St. Louis, MO, USA), 10-min ultrasonic cleaning with isopropyl alcohol 99% (CAS 67-63-0, Pharmco Aaper, Bookfield, CT, USA), vigorous rinsing with deionized (DI) water for 1 min, and drying with high-purity-grade nitrogen. [22].

4.1.2 Surface Characterization

Table 4.1 shows the surface cleaning and sample storing methods studied in this work. One sample was used as-is without any further cleaning process; this sample was used as a reference. Two cleaning procedures were studied: cleaning using SCP and cleaning using SCP followed by plasma cleaning with air using a Harrick plasma cleaner (Harrick Plasma, Ithaca, NY) at 18 W for five minutes. The plasma-cleaned samples were exposed to two environmental conditions—(1) in a sealed desiccator at atmospheric pressure and (2) in an open container in normal room conditions (an average relative humidity of 33% and an average temperature of 28 °C).

Table 4.1 Details of the cleaning procedure and storing method of the samples.

Preparation	Sample 1	Sample 2	Sample 3	Sample 4
Cleaning procedure	-	SCP + Plasma	SCP + Plasma	SCP
Storing method	Open container	Open container	Sealed container	Open container

Table 4.2 shows the surface characterization methods that were implemented to study the samples. As the gold-coating quality and glass-slide surface properties may have varied from one sample to another sample, we tried to minimize these effects on the surface characterization results by using a single glass slide for each surface characterization method. A single glass slide was cut into three pieces for AFM measurement, one glass slide was cut into 3 pieces for XPS measurement, and one glass slide was cut into four pieces for contact angle measurement. The surface morphology of samples 2, 3, and 4 at exposure times of 2, 17, 41, 185 h to the atmospheric conditions (exposure time indicates

the duration of time a sample was exposed to the ambient environment after the cleaning process and before the onset of the study) was monitored using AFM. To ensure the repeatability of the result, AFM studies was repeated at three random locations on each sample. The equilibrium contact angle of samples, defined by the mean of the contact angles at five different locations on a sample, was measured by dispensing water droplets with a volume of 0.2–0.5 µL. The contact angle was measured for samples 1, 2, 3, and 4 at exposure times of 0, 4, 18, 46, 180, 1100 h. The surface chemistry of samples was studied by XPS (PHI 5800 X-ray photoelectron spectrometer, Mg X-ray source, $\theta = 45°$).

Table 4.2 Surface characterization methods used to study the surface properties of the samples.

Analysis	Exposure Time (h)			
	Sample 1	Sample 2	Sample 3	Sample 4
XPS	-	0, 4, 17, 43, 180, 893	0, 4, 17, 43, 180, 893	0
AFM	-	2, 17, 41, 185	2, 17, 41, 185	2, 17, 41, 185
Contact Angle	0, 4, 18, 46, 180, 1100	0, 4, 18, 46, 180, 1100	0, 4, 18, 46, 180, 1100	0, 4, 18, 46, 180, 1100
SPRi	-	1~110	1~110	1~110

4.1.3 Adsorbed VOC Characterization Using SPRi

SPRi was used for real-time tracking of adsorbed VOCs on a surface. Our in-house-developed automated SPRi instrument was used for the imaging. Figure 4.1(a) shows a schematic of this instrument. P-polarized monochromatic collimated light required for the SPRi forms by passing a divergent light from a LED illumination system through the optical array (focusing lens, biconvex lens, apertures, 550 nm bandpass filter with a full width-half maximum of 10 nm, and p-polarizer). A stationary mirror and a rotating mirror direct the light to launch on a prism. Reflected light from the prism is guided toward a charge-coupled device (CCD) camera using a second pair of rotating and stationary mirrors. The recorded light contains information on the thickness and refractive index of the medium on top of the gold-coated glass. The use of a motorized rotating and linear stage allows for sweeping the incident angle to obtain the SPRi reflectance curve of a sample. The reflectance curve of the sample reveals the surface plasmon resonance (SPR) angle (the angle corresponding to the minimum reflectance), which works as a fingerprint for characterizing the materials on top of the gold substrate. The characterizations of adsorbed VOCs on samples 2 and 4 were done separately. For each sample, first, the corresponding SPR angle of the sample was found by sweeping the incident angle from 40° to 60°. Then, the incident angle was adjusted to 1.5° below the SPR angle (46.3°), i.e., 44.8°, and the time-lapse images (one frame per 1 min) of each sample were recorded for 110 h at room conditions (relative humidity of 33% and temperature of 28 °C), Figure 4.1(b). To ensure the repeatability of the result, SPRi was repeated three times for sample 2 and sample 4. The schematic of the SPRi of dropwise condensation is illustrated in Figure 4.1(c). First, the reflectance curve for a sample cleaned with SCP was obtained using SPRi wit(b)zh angle-scanning. Then, the incident angle was fixed at 44.8° and the setup was prepared for the SPRi of dropwise condensation at 3000 FPS. For inducing condensation

on the sample, we placed an indium tin oxide (ITO)-coated glass slide as a heater at a distance of 5 mm above the gold surface. A water column (between the heater and the gold-coated glass) with a size of 15 ± 5 µm was formed using a syringe. By heating the water column, part of the water column evaporated and condensed on the surface. The temperature and relative humidity above the study area were 45 °C and $60 \pm 4\%$, respectively, while the condensing surface temperature was 35 °C. The details of the dropwise condensation experiment, image processing, statistical noise analysis, uncertainty of SPRi, and a monolayer water film measurement are discussed elsewhere [5,23,24].

(a)

(b)   (c)

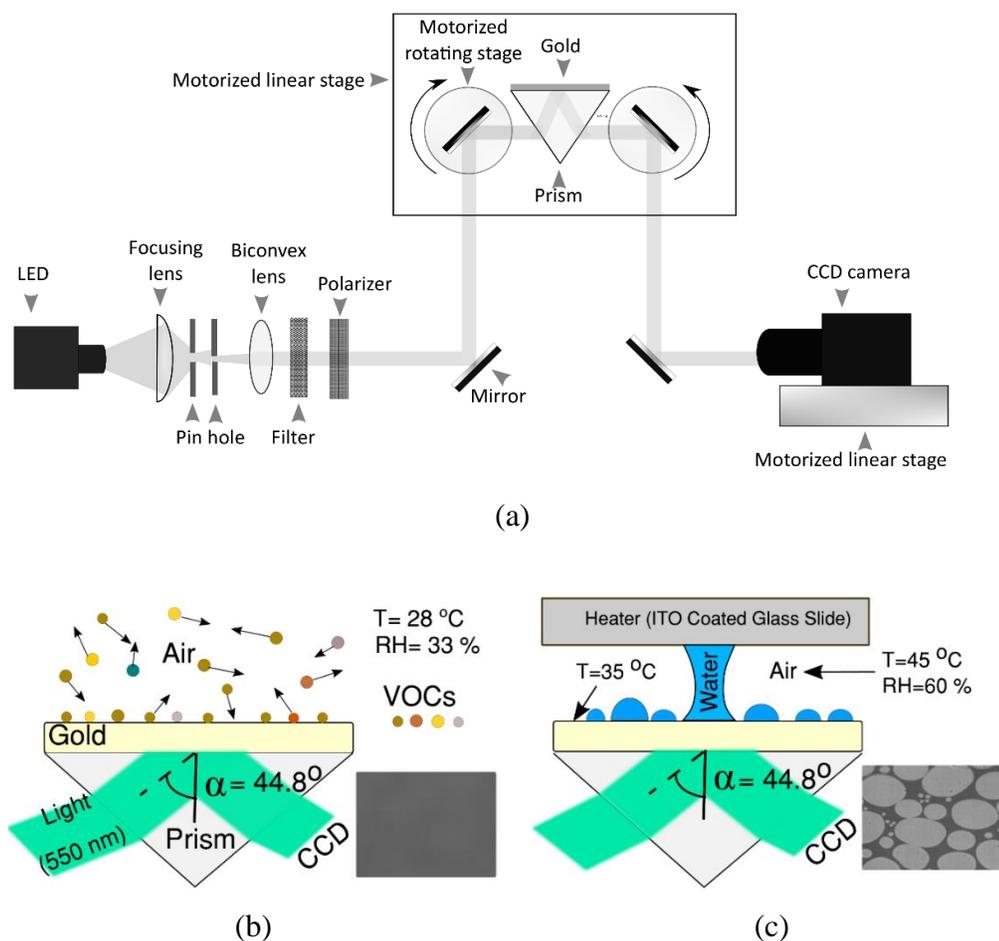Figure 4.1 (a) Schematic of the automated surface plasmon resonance imaging (SPRi) instrument (a p-polarized monochromatic (550 nm) collimated light was used for SPRi), (b) schematic of volatile organic compound (VOC) adsorption experiment using SPRi, and (c) experimental conditions for SPRi of dropwise condensation (brighter color represents droplets and darker color represents the gold substrate).

4.2 Results and Discussion

4.2.1 Proper Cleaning Procedure Prior to the Dropwise Condensation Experiment

Surface defects [7–9] and adsorbed VOCs [10–12] on a surface are key factors that contribute to surface heterogeneity. Surface heterogeneity can cause abnormality in the mechanism of dropwise condensation on a smooth surface. As our final goal was to study the effect of surface treatment on the measurement of ultrathin water film during the dropwise condensation process on a smooth surface, we studied the effect of surface cleaning methods on the surface properties (surface uniformity, surface wettability, and surface chemistry). Figure 4.2(a) and (b) show the surface morphologies of sample 2 with exposure times of 2 h and 185 h, respectively. The root-mean-square of the surface roughness for samples 2 and 3 was reduced slightly (within 183 h exposure time) from 1.10 $\pm$ 0.02 nm to 0.95 $\pm$ 0.10 nm and from 1.14 $\pm$ 0.02 nm to 0.83 $\pm$ 0.06 nm, respectively. Meanwhile, the root-mean-square of surface roughness for sample 4 changed from 1.57 $\pm$ 0.01 nm to 1.70 $\pm$ 0.1 nm. The AFM analysis showed that the surface had a uniform, smooth coating. However, the error of measurement (based on three measurements at three different locations of each sample) increased for all three samples over time. This showed that the adsorption of contamination on the surface can slightly affected the homogeneity of the surface. As the associated error was smaller than 0.10 nm over the course of 183 h, we can consider these samples to have had a uniform surface structure. Figure 4.2(b) shows a defect on the surface of the gold-coated glass; a defect can cause heterogeneous nucleation during the dropwise condensation process [9]. It can be seen in the example case in Figure 4.2(c) that atomic-scale defects and surface edges on the gold-coated glass caused heterogeneous nucleation on the surface (bright spots are micro-size droplets; the darker color represents the gold substrate). This image was recorded at the onset of dropwise condensation using SPRi [23]. As the surface defects were limited on the gold-coated glass surface, and these defects were prescreened prior to the dropwise condensation experiments, the presumption of homogenous nucleation due to the smooth condensing surface is reasonable.

(a) (b)
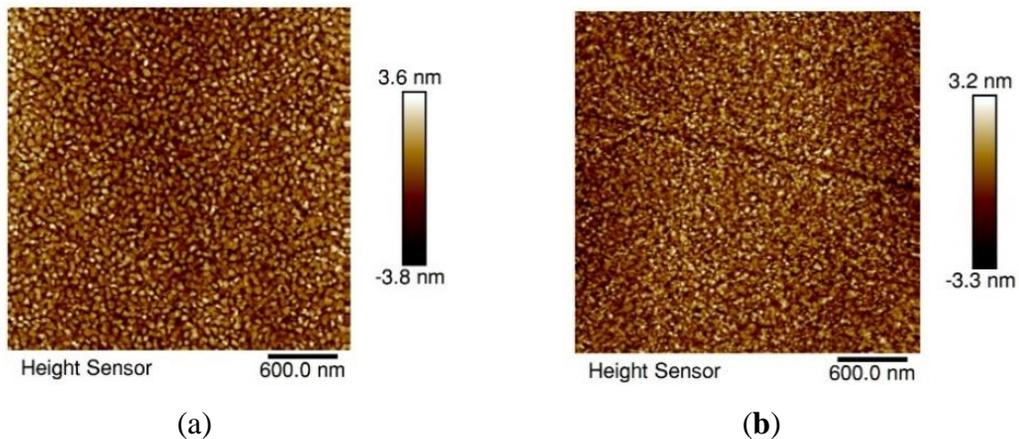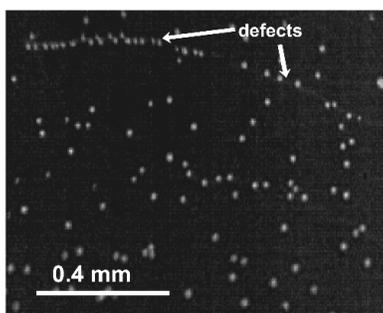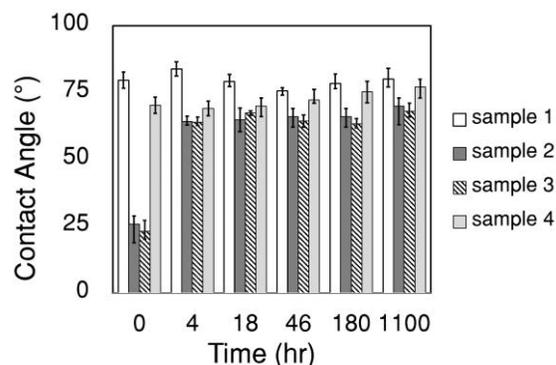
(**c**)   (**d**)

Figure 4.2 AFM images of the sample 2 surface (gold-coated glass, plasma-cleaned and stored in an open container at room conditions) after exposure times of (a) 2 h and (b) 185 h, (c) SPRi of dropwise condensation (the darker color represents the gold substrate and the brighter color shows the droplets) shows surface defects can cause heterogeneous nucleation, and (d) contact angle measurements of the samples.

Equilibrium contact angles of DI water drops on the gold surface are shown in Figure 4.2(d). The averaged contact angle for sample 1 remained relatively constant at 79.4° over the 1100 h period. The contact angle variations over the exposure time of 1100 h were more significant for plasma-cleaned samples –sample 2 (contact angle increased exponentially from 27° to 70°) and sample 3 (contact angle increased exponentially from 23° to 68°). For sample 4, which was cleaned with the SCP, the averaged static contact angle was slightly increased (from 70° to 76°) in 1100 h. The results showed that the cleaned samples had smaller contact angles, as compared to the sample with no surface cleaning (sample 1). The decrease of contact angle after surface cleaning could have been an indication of removing some adsorbed VOCs from the surface. The variations in the contact angles were more significant (~ 44°) in the plasma-cleaned samples.

To understand the mechanism of increased hydrophobicity in the plasma-cleaned samples, we analyzed the variation in surface chemistry using XPS. A broad-range energy scan of the cleaned samples showed the presence of gold (Au 4f), carbon (C 1s), and oxygen (O 1s) on the samples' surface, see Figure 4.3(a). High-resolution XPS spectra of C 1s and O 1s indicated that the atomic parentage of C 1s and O 1s increased significantly on the plasma-cleaned surfaces during the one-month exposure time, see Figure 4.3(b). For sample 2, the ratio of C/Au, which is the indicator of adsorbed VOCs, increased by 240% during the exposure time of one month. The result showed the amount of non-polar C–C (or C–H), which is responsible for hydrophobicity, was the dominant part (76%) of the adsorbed hydrocarbons. The high-resolution XPS spectra of sample 4 (seen in Figure 4.3(c)) revealed that the adsorbed VOCs on the surface did not contain a polar C=O bond that causes hydrophilicity on the surface. This could explain the larger contact angle (76°) of sample 4 cleaned with SCP, as compared with the eventual contact angle (70° after an 1100 h exposure time) of sample 2. Based on the surface characterizations of samples, we

39

used SCP as the cleaning procedure for the gold samples before the condensation experiment. SCP produced negligible changes to the chemistry of the surface, as compared to the plasma cleaning method. Therefore, the effect of concurrent adsorption of VOCs during the condensation experiment, which can take up to several hours after the cleaning process, was expected to be less than that of the samples treated with the plasma cleaning method.
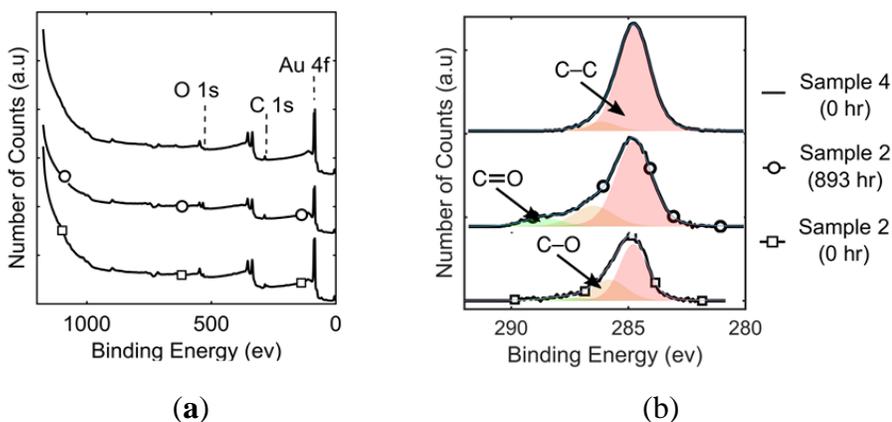
Figure 4.3 (a) Broad-range energy scan and (b) high-resolution XPS spectra of sample 2 (exposure time of 0 and 893 h) and sample 4 (exposure time of 0 h).

4.2.2 Proper Storing Methods of Gold-Coated Samples

As the samples–in our study, gold-coated glass–are usually fabricated in batches weeks or months before the experiment, it is important to properly store them to minimize the amount of absorbed contaminations (as a result, surface heterogenicity) on the samples' surface. Samples 2 and 3 cut from the same glass slide were both cleaned by SCP, followed by air plasma cleaning. Therefore, the initial conditions for both of these samples should have been relatively similar. As Table 4.2 shows, sample 2 was kept in an open container in an area of a laboratory that is less accessible by personnel (an average relative humidity of 33% and an average temperature of 28 °C). Further, sample 3 was placed in a sealed desiccator. The AFM results showed the roughness of the two samples were relatively similar during the 185 h exposure time. The contact angle results show a similar trend in the increase of contact angle (44° increase in 1100 h). The atomic percentage of O 1s, C 1s, and Au 4f from XPS are depicted in Figure 4.4 for samples 2 and 3. The results indicate that the atomic percentage of C 1s changed from ~ 24% to 40% in one month for both samples, while the atomic percentage of O 1s in sample 2 increased from 7% to 15% and the atomic percentage of O 1s in sample 3 decreased from 10% to 8%. As a result, the atomic percentage of Au 4f was 10% more for the sample kept in a sealed desiccator (sample 3) compared to the sample kept in the open container (sample 2). This result showed that the amount of adsorbed VOCs can be decreased on the surface when the samples are kept in a sealed desiccator. This storing method can be very important for optical microscopies, such as SPRi or ellipsometry, which are sensitive to atomic variations in the thickness of samples.
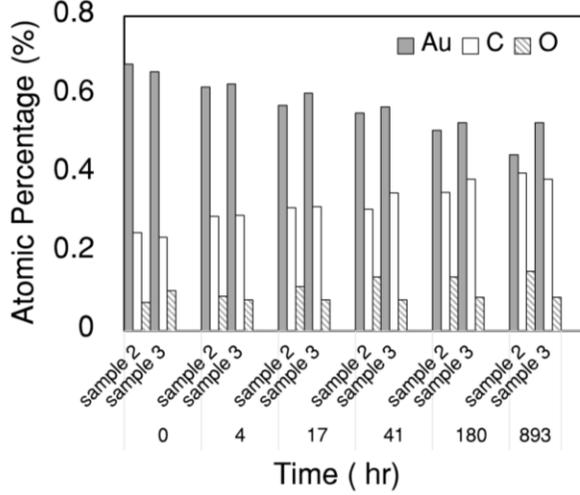
Figure 4.4 The sample stored in a desiccator (sample 3) allowed adsorption of fewer VOC molecules—a higher atomic percentage of Au—on its surface, as compared to the samples left in an open environment (sample 2) by desorbing the part of VOCs that has double oxygen bonds.

4.2.3 The Effect of Adsorption of VOCs on SPR Reflectance

As Figure 4.1(a) and (b) show, the recorded images from SPRi are in grayscale (with pixel intensity values in the range of 0 to 4940). For the quantitative analysis of the results, it is required to normalize the images by converting the pixel intensity value into units of reflectivity (0–1). Reflectivity units show the ratio of reflected light from the prism into the incident light on the prism and allow comparison between the SPR theoretical model and the experimental result. The theoretical SPR reflectance can be modeled by solving the Fresnel equation for transverse magnetic light (p-polarized light) in a four-layer configuration BK7 prism, gold, water, and air as:

$$R_{SPR} = \frac{r_{12}[1+\exp(-2i\ K_2 d_2)]+[r_{12}r_{23}+\exp(-2i\ K_2 d_2)]r_{34}\exp(-2K_3 d_3)}{1+r_{12}r_{23}\exp(-2i\ K_2 d_2)+[r_{23}+r_{12}\exp(-2i\ K_2 d_2)]r_{34}\exp(-2K_3 d_3)}$$ (4.1)

In this equation, the thickness of the air and the BK7 prism are considered infinity, and the thickness of the gold layer is 50 nm. In the case of SPRi of adsorbed VOCs on the surface, the thickness of the water layer is zero and Equation (1) reduces into the three-layer system. It is important to note that we assume the initial thickness of adsorbed VOCs on the surface is zero on the surface. For normalization of images, we introduced a scaling factor:

$$S = \frac{I_{SPR,\ max} - I_{SPR,\ min}}{R_{SPR,t,\ max} - R_{SPR,t,\ min}}$$ (4.2)

At a wavelength of 550 nm, the $R_{SPR,\ t,\ max}$ and $R_{SPR,\ t,\ min}$ were, respectively, 0.778 (at α = 42.0°) and 0.089 (at α = 46.3°) from theoretical reflectance–angle plot. The reflectivity at each pixel can be calculated using:

41

$$C = I_{SPR, \, max} - S \, R_{SPR,t, \, min}$$
(4.3)

$$R_{SPR} = (1 - C) / S + R_{SPR,t, \, min}$$
(4.4)

The reflectance–incident angle curves for samples 2 and 4 are shown in Figure 4.5 (a) and (b), respectively. The results show a good agreement between theoretical and experimental results. The real-time effects of adsorbed VOCs on the SPR reflectivity were measured by visualizing changes in the reflectivity of the surface at a fixed incident angle of 44.8°. This angle is the same angle we used for observation of dropwise condensation. Figure 4.5(a) shows the reflectance changes with time for sample 2. The result indicates an odd behavior; initially, (for the first 43 h) reflectance dropped significantly (~ 5%). In the next 70 h, reflectance gradually increased (1%). The SPRi was set up in such a way (incident angle of 44.8° and wavelength of 550 nm [5]) that any increase in the reflectance showed an increase in the thickness of the adsorbed layer and/or an increase in the refractive index of the adsorbed layer. Conversely, a decrease in the reflectance is an indicator of desorption and/or reduction in the refractive index of the adsorbed layer. As SPRi was performed under intensity modulation, it was not possible to deconvolute changes in the refractive index and the thickness of the adsorbed layer concurrently. Simultaneous measurement of refractive index and thickness of a film using SPRi is possible when SPRi with angle-scanning is performed at two different wavelengths. It is possible to determine refractive index and thickness of sample from Equation (1) using reflectance–incident angle curve at two wavelengths. More information regarding the simultaneous measurement of refractive index and thickness can be found in our previous work [24]. In this work, we used XPS data to observe the trend of the adsorbed layer thickness with time. For a two-layer (overlayer and substrate) structure where the overlayer does not produce electrons with the binding energy of interest, i.e., the overlayer does not produce photoelectrons with the binding energy of Au 4f, the thickness (d_{over}) of the adsorbed VOCs on the gold surface can be estimated from XPS data [25]:

$$I_{XPS} = I_{XPS, \, sub} \exp(\frac{-d_{over}}{\lambda \cos \theta})$$
(4.5)

For a thick substrate ($d_{sub} \gg \lambda$), $I_{XPS, \, sub}$ can be considered as I_{∞}, the intensity of a thick sublayer without an overlayer. This is the case for our surface as the 50 nm thick gold layer is much greater than the electron attenuation length of Au 4f photoelectrons (3 nm) through gold.
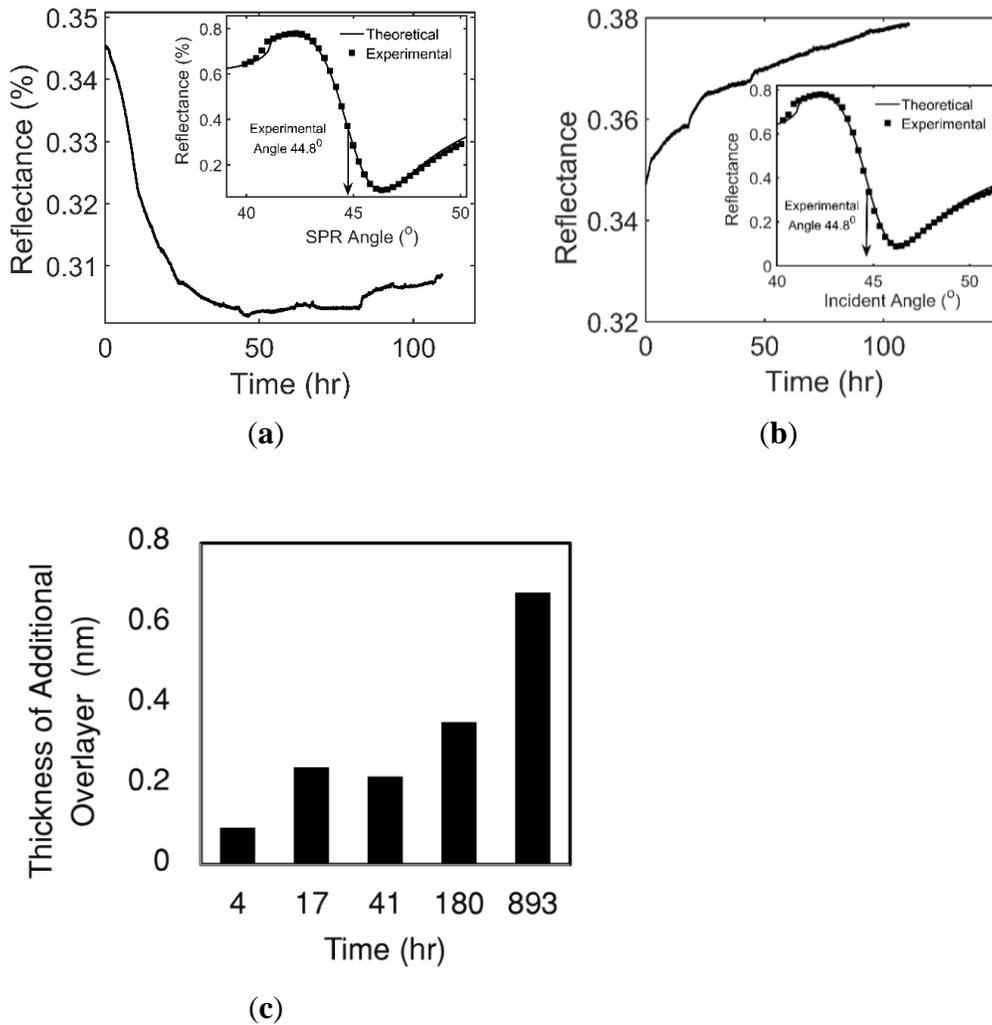
Figure 4.5 SPRi results of (a) sample 2 and (b) sample 4 (the inner plots show the angle-scanning result, and the outer curve shows the effect of adsorbed VOCs on the SPR signal at 44.8°) and (c) XPS result of sample 2 shows the trend of adsorbed VOCs layer thickness variation.

I_∞ is usually measured directly. Normally, for a metal substrate such as gold, the surface is argon sputtered in the XPS chamber to get the signal without the overlayer. However, our samples were not argon sputtered in the XPS chamber and they had a small overlayer at the beginning. Argon sputtering was not been implemented as it would likely have affected the surface morphology and homogeneity of the surface [26] (for studying the mechanism of dropwise condensation, the surface needs to be smooth). The initial overlayer in the first measurement can be seen by the presence of C 1s in the broad range scan of samples (see Figure 4.3). Therefore, our thickness measurement was an estimate of the additional overlayer thickness formed after the initial measurement and not the actual overlayer thickness. By changing the order of Equation (1):

$$d_{over} = -\ln\left(\frac{I_{XPS}}{I_{XPS,\,0}}\right) \lambda \cos\eta \qquad\qquad (4.6)$$

where $I_{XPS,\,0}$ is the signal associated with Au 4f generated from the substrate layer during the first measurement (t = 0 h), and the collection angle relative to the surface (η) is 45°. The thickness of the additional overlayer was measured by assuming the adsorbed layer formed a uniform layer on the surface.

Figure 4.5(c) presents the trend of thickness variations in one month for sample 2; the thickness exponentially increased in the first 17 h (from 0 to 0.24 nm), then it dropped slightly at 41 h (from 0.24 nm to 0.22 nm); finally, it increased from 0.22 nm to 0.68 nm at 893 h. As these results are based on a single XPS measurement, we cannot present the error of measurement. The increasing trend in the thickness of adsorbed VOCs means the initial drop in the SPR reflectance was due to a drastic decrease in the refractive index, i.e., the chemistry of the adsorbed VOCs on the plasma-cleaned sample initially changed from compounds with a higher refractive index to compounds with a lower refractive index. As these thickness measurements were estimated, we cannot precisely estimate the changes in the refractive index of the adsorbed layer. It is worth noting that a quantitative calculation of the adsorbed layer's refractive index was not the goal of this work. Therefore, we only mention this to note the trend of changes in the adsorbed VOCs for sample 2. By tracking the atomic percentage of C and O in the XPS data of sample 2, we can understand how the amount of C–O (compared to C–C (C–H) and C=O) in a high-resolution carbon spectrum reduced on the surface for the first 41 h and then increased. Further, XPS data indicated that the peak binding energy of O-C (in high-resolution oxygen spectrum) changed from 533.08 eV to 532.6 eV in 41 h and bounced back to 532.93 eV in the one-month period. The O–C peak shift and atomic percentage can be deciphered as adsorbed VOCs changing from aromatic hydrocarbons to aliphatic hydrocarbons in the first 41 h after exposure. The reflectance behavior of the plasma-cleaned sample clearly showed this method of surface cleaning is not a proper method for SPRi, as it can complicate the interpretation of the SPR results.

The SPRi of samples cleaned with SCP (sample 4) showed a 4% increase of reflectance in 110 h, as shown in Figure 4.5 (b). To estimate the thickness of the adsorbed layer, we assumed a range of refractive indices from 1. 33 to 1.4 as the refractive index of adsorbed VOCS. This range of refractive indices represents a variety of organic hydrocarbons [27]. Hence, the reflectance of 4% showed the formation of a 0.85–1 nm adsorbed layer. As adsorption of VOCs is inevitable during the experiment involving ultrathin film (<1 nm) measurement, it is imperative to quantify any uncertainties associated with the adsorption of VOCs. Recently, we have shown the existence of a monolayer thin film between droplets during the dropwise condensation process on a gold-coated glass [5]. The results of our work can shed new light on the mechanism of dropwise condensation, which has been under debate for more than nine decades. Here, we focus on the effect of adsorbed VOCs on a monolayer thin film measurement. The SPRi of dropwise condensation took less than an hour. As a result, the net effect of adsorbed VOCs on the reflectance can be estimated from Figure 4.5(a) as 0.0025 (reflectivity unit) or 0.053–0.0625 nm (thickness depends on the index) during the one-hour experiment. It is worth noting that our experiment on the

effect of adsorbed VOCs on the SPR reflectance was conducted at lower relative humidity and temperature, as compared to the environmental conditions of the dropwise condensation experiment. It has been shown that the adsorption of VOCs reduces with increasing relative humidity and temperature. Therefore, the net effect of adsorbed VOCs on SPR reflectance during the dropwise condensation experiment should be smaller than 0.0025 (reflectivity unit) or 0.0625 nm [28–30]. This value is only 30% of the reflectance measured from a monolayer film of water (i.e., the corresponding reflectance is 0.0082) during the dropwise condensation experiment. Quantification of adsorbed VOCs on the SPRi signal helps us to confidently claim that the monolayer film that we have experimentally observed represents an adsorbed water film. Therefore, the adsorbed film exists between droplets during the dropwise condensation. The next questions that needs to be answered by researchers are whether this thin film plays any role in the growth of nucleates and whether this film can affect the overall heat transfer rate. If the answers to these questions are positive, the future models of dropwise condensation need to be revised accordingly.

4.3 Conclusions

The existence and thickness of a thin film between droplets during the dropwise condensation process has been under debate for decades. In a recent article published by the authors, we shared our observation (using SPRi) of a monolayer-thick water film that exists between the droplets on a smooth hydrophilic condensing surface. As the thickness of this ultrathin film can be similar to the thickness of the adsorbed VOCs layer that forms on the surface during the dropwise condensation experiment, we used two surface-treatment processes–SCP and air plasma cleaning–and four surface characterization techniques–AFM, optical microscopy, XPS, and SPRi–to quantify the effect of adsorbed VOCs during the dropwise condensation experiment. The results indicate that (1) both surface cleaning methods have negligible effects on surface homogeneity, (2) neither method fully removes the adsorbed VOCs from the surface, (3) the rate of adsorption of VOCs after plasma cleaning is high and it can cause up to 5% change in the SPR signal, (4) the SCP is recommended prior to sensitive measurement such as ultrathin film (<1nm) measurement using SPRi due to its minimal effect on the SPR reflectance, and (5) the thickness of adsorbed VOCs is more than 70% smaller than the thickness of the monolayer film that is observed between the droplets during the dropwise condensation on a gold-coated glass. This finding verifies our claim [5,6] that a thin water film exists during dropwise condensation.

5 Dropwise Condensation Mechanism on Smooth Hydrophilic Surface

Dropwise condensation has the potential to improve efficiency and reduce maintenance costs of heat transfer systems. However, efforts to design and fabricate surfaces to sustain long-term dropwise condensation have not been successful [68, 103]. The main reason is that the physics behind dropwise condensation is not fully understood [27]. Currently, there are two competing theories on the mechanism of dropwise condensation: classical nucleation and film rupture theories [69]. Nucleation theory was first introduced by Tammann and Boehme in 1935 [26]. This theory claims that droplets nucleate heterogeneously on the surface. Then, the droplets grow and coalesce to make larger droplets. Heat transfer is dominant through the droplets (defined as the active area) and the area between the droplets is considered inactive. Umur and Griffith [23] experimentally showed nucleation theory is the mechanism of dropwise condensation. They studied the static dropwise condensation of steam on gold surface and showed no film larger than a monolayer exists between droplets. Therefore, their finding supports the area between droplets is not active in heat transfer. The majority of researchers support nucleation theory as the governing mechanism of dropwise condensation [104]. Numerical models that have been developed to predict dropwise condensation are mostly based on nucleation physics [27, 105].

Film rupture theory was first introduced in 1937 by Jacob et al. [24]. This theory hypothesized that vapor condenses as a thin film on the surface. At a critical thickness, the thin film breaks up and small droplets form on the surface. According to this theory, a thin film (e.g., a film with thickness larger than a monolayer) exists between droplets. Song et al. [21]argued that dropwise conduction is a dynamic process. Therefore, the static dropwise condensation experiment conducted by Umar and Griffith [23] could not represent the actual dropwise condensation process. Song et al. showed experimentally the presence of thin film between droplets during the dynamic dropwise condensation of steam on a steel surface.

The work of Umar and Griffith [23] is one of the main experimental studies that support the nucleation theory and the research of Song et al. [21] is one of the main supporters of film rupture theory. These conflicting experimental works are the main reason for existing of two competing theories on the mechanism of dropwise condensation. In this work, we study the dropwise condensation mechanism by conducting similar experiments to the works of Umar and Griffith [101]and Song et al. [21].

Due to the need for visualization of interfacial phenomena with high-frequency features, such as ultrathin film instabilities, we developed an automated SPRi instrument, the first-ever reported instrument capable of imaging a sub-nanometer film at high-speed (up to 10,000 FPS) in ambient conditions [1]. This developed near-field imaging system was applied [1-3, 106] to understand the physics of dropwise condensation under debate for the past nine decades [69]. We interpret the static dropwise condensation in Umar and Griffith work [23] as stable dropwise condensation (SDC) occurring at a very low condensation rate. SDC is a dropwise condensation that can be sustained on the surface for a long-time.

Here, the droplet growth rate of 1 µm/s in diameter allows us to conduct SDC on the gold-coated glass. Our interpretation from the dynamic dropwise condensation of steam mentioned in Song et al. work [21] is unstable dropwise condensation (UDC) on a hydrophilic surface. UDC is a dropwise condensation that degrades over time and eventually turns into film wise condensation. In this work, UDC of steam was conducted at a droplet growth rate of 20 µm/s in diameter on a gold-coated glass.

5.1 Experimental Procedure

The visualization of dropwise condensation was carried by SPRi instrument. The SPR instrument used for this study was an in-house developed microscope [1]. The schematics of dropwise condensation experiments are detailed in Figure **5.1**. The substrate is 50 nm gold with 2.5 nm of titanium as an adhesive layer coated on a glass substrate. SDC was conducted at the droplet growth rate of 1 µm/s in diameter. As Figure 1(a) shows an ITO-coated glass is placed 4-5 mm above the gold surface as a heater and a water column with a volume of 10-15 µl is formed between the substrate and the heater. By heating the water bridge the water evaporates and condenses on the gold surface. During the visualization of dropwise condensation, the temperature of the gold surface was at 35 ℃, the local temperature of air above the gold surface was at 45 ℃, and the RH was at 60 %. The thermocouples are not shown in the schematics of Figure 5.1. In the case of UDC, a 3-D printed chamber with an inlet and outlet is placed on top of the gold surface as an enclosure (see Figure **5.1** (b)). The relative humidity (RH= 99 %) and temperature (T = 97 ℃) are monitored inside the enclosure using one temperature and relative humidity sensor (DHT22 sensor based on ArduinoMega 2560 controller). The steam was introduced into the chamber from the inlet and vent from the outlet of the chamber. As dropwise condensation of steam occurs on a smooth gold surface and no drainage mechanism was designed for this surface, it is intuitive to see the degradation of dropwise condensation in the long term. The SPRi visualization was carried out at 550 nm and 680 nm for both stable and unstable dropwise condensation. More details about the experimental procedure, visualization, and analysis of data are provided in our previous work [1].
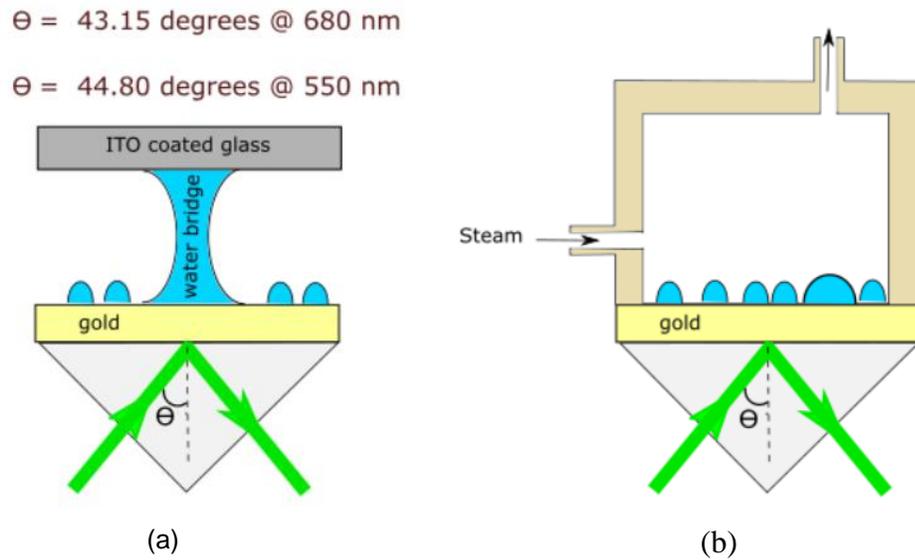
Figure 5.1 (a) Schematic of experimental setup for stable dropwise condensation and (b) schematic of experimental setup for unstable drpwise condensation.

In the case of SDC at the RH of 60%, the condensation rate was approximately 0.0009 $\mu l/(mm^2 s)$, or a heat transfer rate of 0.2 W/cm^2. The droplet growth rate was roughly calculated to be around 1 $\mu m/s$ in diameter. In the case of UDC, the droplet growth rate was calculated roughly to be around 20 $\mu m/s$ in diameter. SDC and UDC were repeated 3-5 times at both wavelengths of 680 nm and 550 nm. The camera was set up at 43.15 degrees (0.15 degrees below SPR angle for air at 680 nm) and 44.80 degrees (1.5 degrees below SPR angle of air at 550 nm), respectively for SPRi with intensity modulation at 680 nm and 550 nm. Figure 5.2 shows the theoretical reflectance curve for SPRi of a 1 nm layer of water at wavelengths of 550 nm and 680 nm. The experimental angles shown in these plots are the incident angle of 44.80 degrees and 43.15 degrees respectively implemented for SPRi with intensity modulation at 550 nm and 680 nm. At 550 nm and experimental angle of 44.80 degrees, a 1 nm water film can result in a ~ 4 % change in the reflectance of the recorded signal. While at 680 nm and experimental angle of 43.15 degrees, a 1 nm of water on the gold surface can produce ~16 % change in the reflectance. Therefore, SPRi with a higher wavelength provides a better resolution in measuring ultrathin films. On the other hand, SPRi at 550 nm provides a better lateral resolution for our imaging; The lateral resolutions at 550 nm and 680 nm respectively are 4 μm and 10 μm. Because of the trade-off in resolutions, we repeated the dropwise condensation experiments at both wavelengths of 550 nm and 680 nm.

(a)　　　　　　　　　　　　　　　(b)
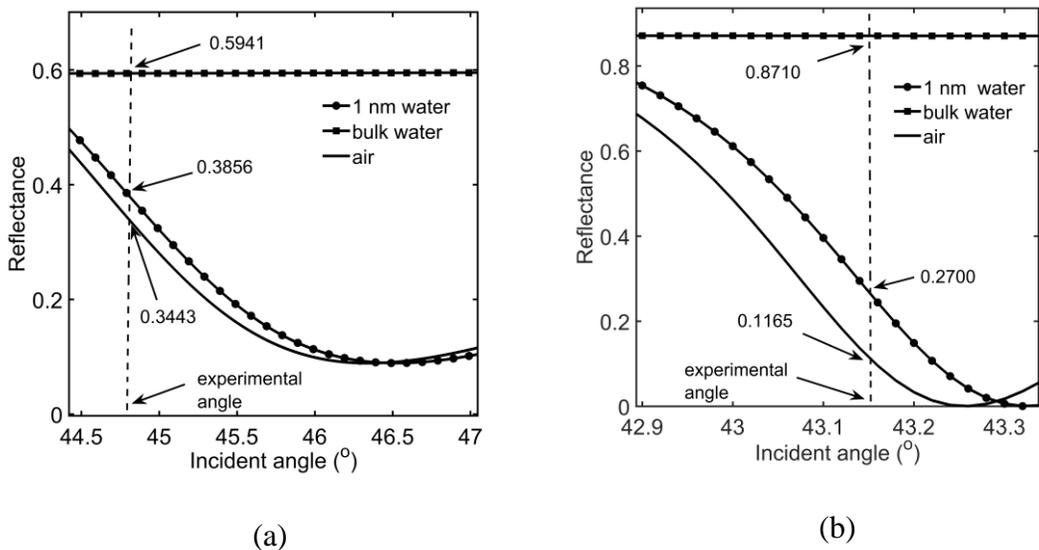
Figure 5.2 Theoretical SPR plots showing the effect of 1 nm water film on the reflectance at (a) 550 nm and (b) 680 nm.

5.2 Results and Discussions

5.2.1 Onset of SDC

As SPR imaging is a powerful technique in the detection of thin films, we designed our experiment to understand whether thin film can be detected at the onset of dropwise condensation.
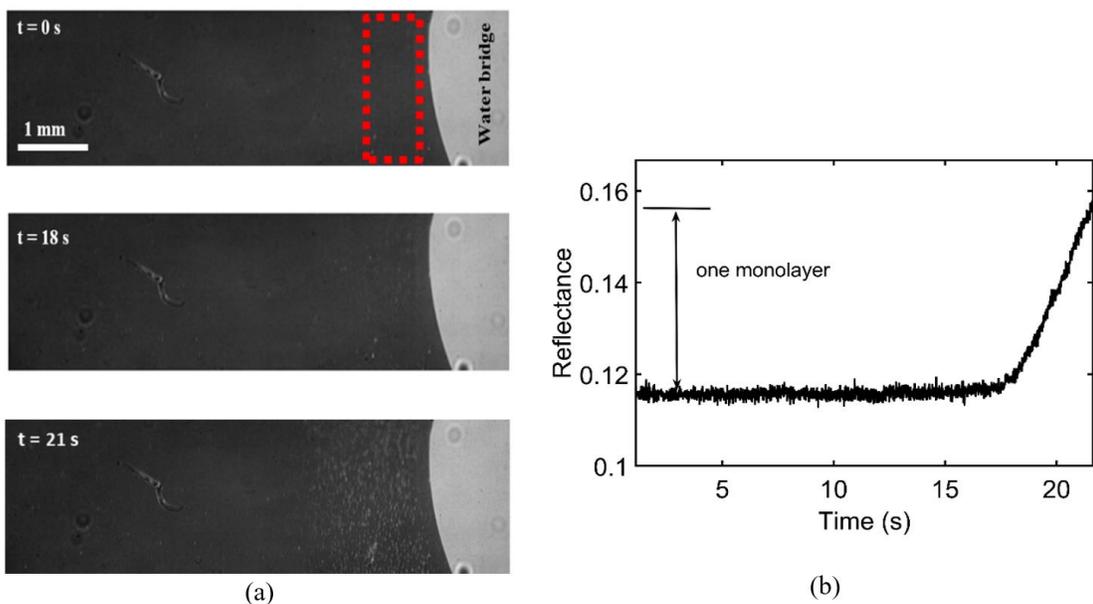

(a)　　　　　　　　　　　　　　　(b)

Figure 5.3 (a) shows the SPRi (at 680 nm) results of SDC at the onset of condensation. Online Resource 1 shows the corresponding video of SDC at 680 nm. The light gray and dark gray respectively represent water and gold surface. The visualization of the surface starts at 0 s, after about 6 seconds The first droplets form on the surface after 18 s from the start of visualization. The reflectance variation is measured by tracking the averaged reflectance of pixels in the red dotted box with time. The location of red dotted box is chosen in vicinity of water bridge as the initial droplets emerge on part of the surface that is closer to the location of water bridge. As aforementioned, the formation of a water film with the thickness of a molecule layer corresponds to a 4% change in the measured reflectance. However, the result indicates reflectance variations before the emergence of the first droplets is infinitesimal (see Figure 5.3 (b)). This means no film even as small as a molecule layer forms on the surface prior to the emergence of droplets at the onset of SDC i.e., the initial droplets form by heterogeneous nucleation on the surface. In our other work [1], we showed the area between droplets are covered with a monolayer film during SDC. Our results confirm the finding of Umur and Griffith [23] in support of nucleation theory as the mechanism of dropwise condensation.

.

(a)   (b)
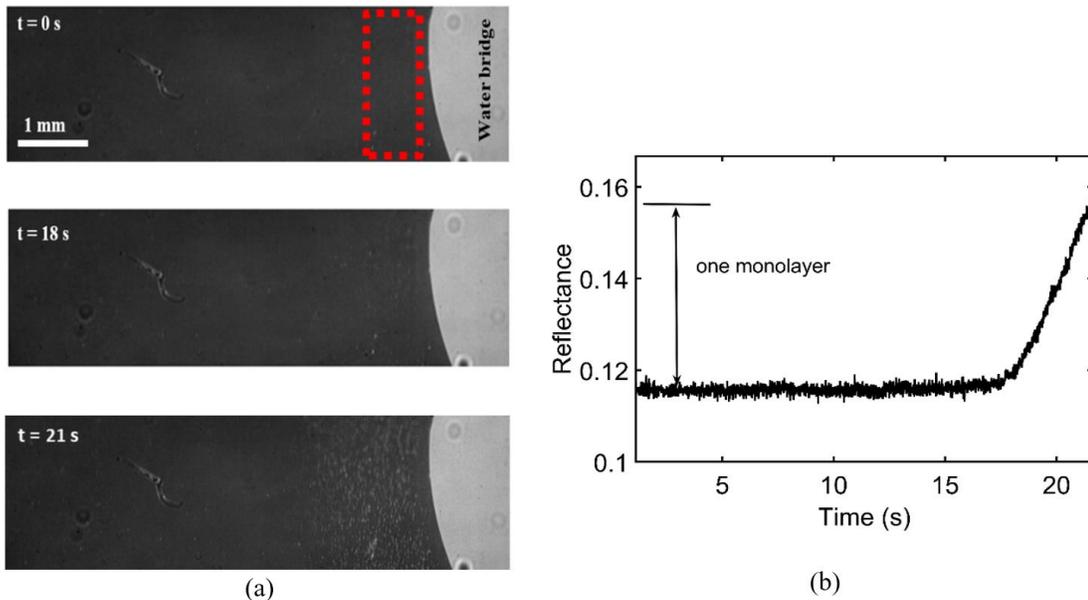
Figure 5.3 Time-lapse images recorded using SPRi at 680 nm from the onset of SDC shows no thin film forms on the surface prior to the droplet formation.

In a different set of experiments, the water bridge on the surface was slightly relocated on the surface. After ~16 s, SDC was conducted by heating the water bridge using the ITO coated glass. Figure 5.4 shows time-lapse images of this experiment recorded using SPRi at 550 nm. The relocation of water bridge on the surface left behind an area with a lower reflectance compared to the rest of the surface. As Figure 5.4 (b) shows the area which was previously occupied by the water bridge (location 1) can be identified with its darker gray color from the rest of the surface (location 2). Our analysis shows the reflectance of location 2 is 1% higher than the reflectance of location 1, i.e., for ambient conditions, the gold

surface founds to be fully covered with a molecule layer of adsorbed water. Figure 5.4 (f) shows the temporal changes of reflectance at locations 1 and 2. It can be observed the rate of water adsorption on the surface increased with the start of SDC. The increase in RH after condensation (from 35 % to 60 %) and the increase in temperature (from 25 °C to 45 °C) lead to an increase in the rate of water molecules striking the surface and consequently increase the rate of formation of the adsorbed monolayer in location 1. The visualization also illustrates that nucleation due to dropwise condensation occurs on the preoccupied area even before the completion of adsorbed monolayer formation (See Figure 5.4 (c) and (d)). It is worth noting that the adsorbed water molecules on the surface mostly consist of water molecules and not volatile organic compounds (VOCs). In chapter 4, it is shown the rate of adsorption of VOCs on the gold surface is much slower than the rate of adsorption of the molecularly adsorbed water layer on the surface [3].
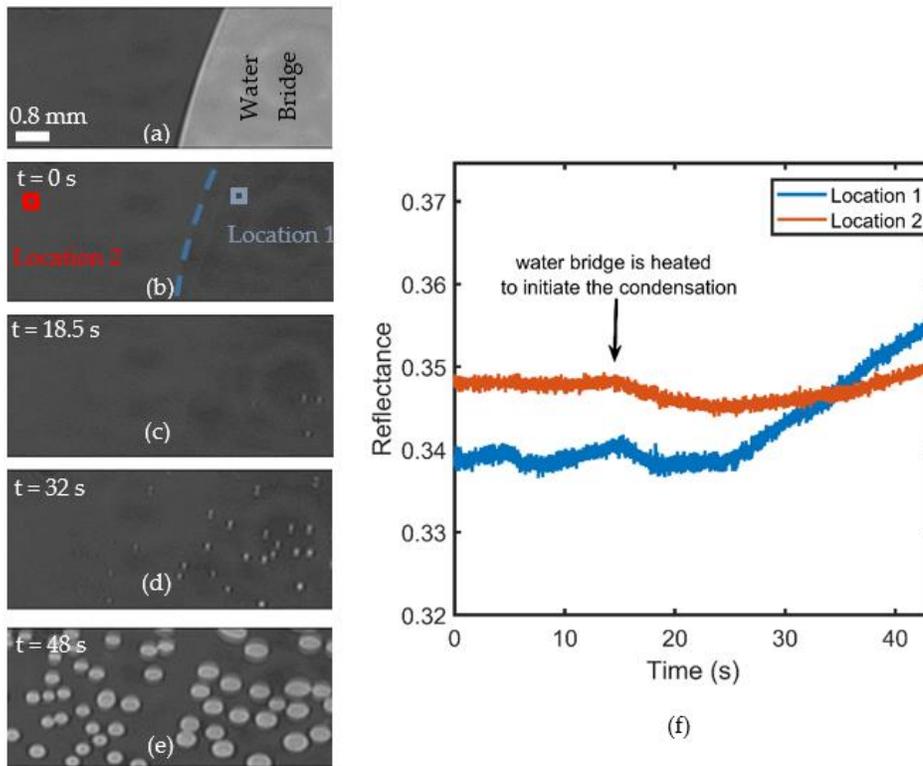
Figure 5.4 (a) Water bridge on the gold surface, (b) relocation of water bridge leaving behind an area that is darker in color; the gold surface in ambient condition (location 2) is covered with a monolayer of adsorbed water, (c)(d)(e) time-lapse images of dropwise condensation on the surface, and (f) the reflectance of location 2 remained relatively constant while reflectance of location 1 increased.

5.2.2 Visualization of UDC

Song et al. [21] did not use any drainage mechanism on their condensing surface. Similarly, we have not considered any drainage mechanism on the gold surface. Therefore, it is intuitive to expect the dropwise condensation to degrade with time in our experiments. We

break down the UDC into three stages: onset of condensation, growth of multilayer film up to 8 nm, and thin-film growth more than 8 nm. These stages are separated by the presence and/or size of the thin film between droplets. The 8 nm is the maximum thickness that is measurable in our SPR imaging.

Figure 5.5 illustrates the recorded images at the onset of UDC experiments. The corresponding video of the onset of UDC is available as Online Resource 2. When steam is introduced to the surface, the vapor molecules in the ambient strikes the surface and form a film-like layer on the surface (see Figure 5.5(a)(b)). This layer propagates from the inlet of steam, i.e., in the example case of Figure 5 from the right side to the left side of the image. Then, the reflectance of this film-like layer increases (up to the reflectance of a droplet which is 0.5941 and 0.8910 respectively for SPRi at 550 nm and 680 nm, see Figure 5.5 (c)), and eventually distinct droplets emerge on the surface (see Figure 5.5 (d)). It can be seen in the example case of Figure 5.5 the distinct droplets also emerge randomly on the surface. The visualization results may look that a thin film forms on the surface and eventually this film ruptures. However, due to low lateral resolution (the lateral resolution is respectively 4 µm and 10 µm at SPRi with 550 nm and 680 nm) of experiments, the visualization can be misleading. In other words, as the size of each pixel is bigger than the size of initial droplets that form on the surface, the colonies of sub-micron size droplets at the onset of condensation can also create an image similar to a thin film. Therefore, the current visualizations cannot provide sufficient evidence regarding the mechanism of droplet formation at the onset of UDC. In our future study, we will equip the SPRi with a high aperture objective lens to study the onset of dropwise condensation of steam with more details.
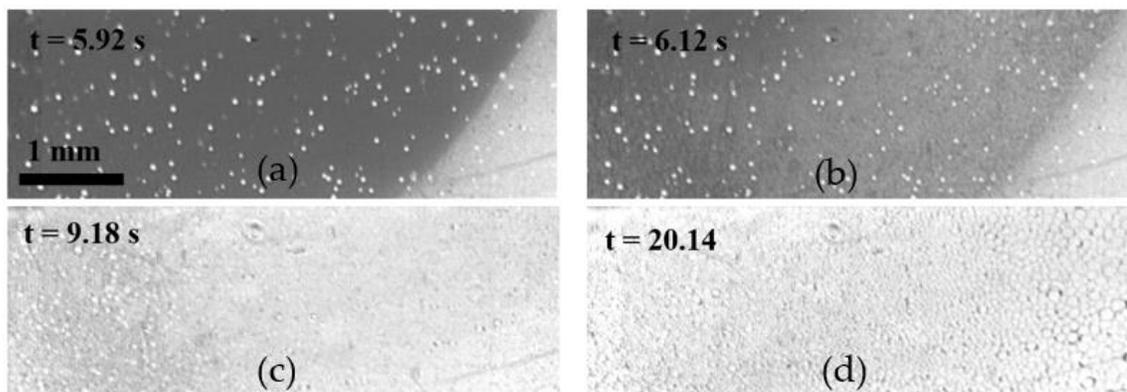
Figure 5.5 Time-lapse images from the onset of UDC provide inconclusive evidence whether thin film larger than a monolayer exist on the surface; the images are recorded using SPRi at 680 nm.

After Stage I, droplets grow and coalesce to create larger droplets. As no drainage mechanism was designed on the condensing surface, it is intuitive to expect the long-term dropwise condensation of steam is not sustainable on the gold surface. At stage II of UDC, the results show the reflectance of the area between droplets increases. The increase in the reflectance indicates the formation of a multilayer molecules water film between droplets.

Figure 5.6 (a) and (b) respectively show the raw image and processed image from stage II of UDC. The dark blue in Figure 5.6 (b) represents water droplets and the thickness of thin-film between droplets varies between 3-6 nm. As the UDC continues, the thickness of thin-

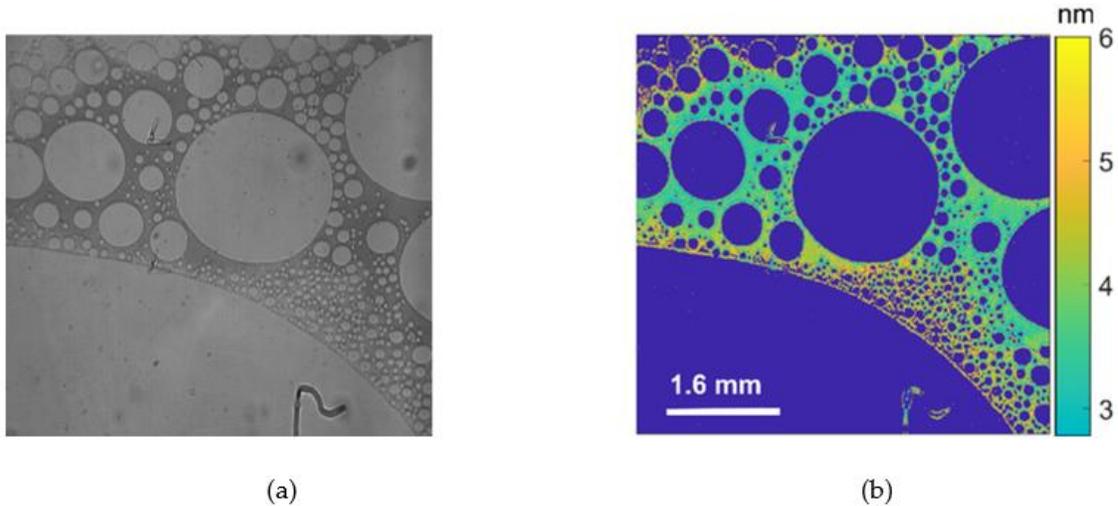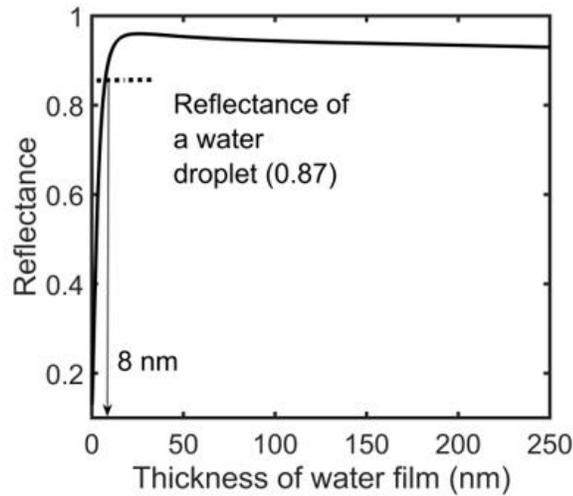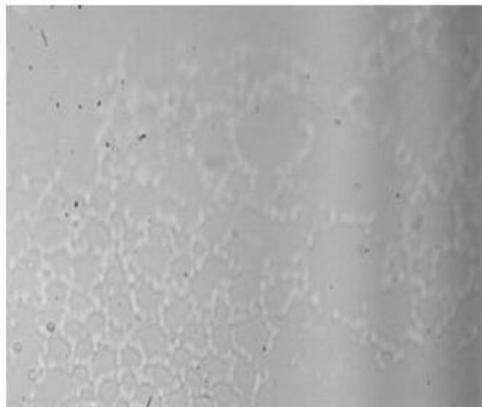(a)   (b)

Figure 5.6 Formation of multilayer water film between droplets during stage II of UDC (a) recorded image using SPRi at 680 nm and (b) processed image with thickness map and dark blue represents the droplet of water.
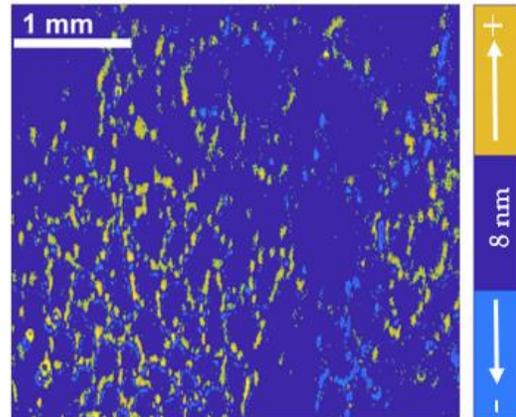
Stage III of UDC is the growth of the thin film between droplets beyond the detection range (> 8 nm) of our SPRi. Figure 5.7 (a) depicts the correlation between the reflectance and thickness of water film for SPRi with IM (experimental angle of 43.15 degrees) at 680 nm. As this figure shows the reflectance associated with just air (no film on the surface) is 0 and the reflectance associated with a liquid droplet on the surface is 0.87. The reflectance of 0 and 0.87 are practically the minimum and maximum reflectance that we can measure using our SPRi. In terms of thin film measurement, the water film with a thickness of 8 nm produces a signal that is equivalent to the reflectance of a water droplet, i.e., reflectance of 0.87. Therefore, the range that we can measure a thin film with is 0 to 8 nm. the If the thickness of thin film goes beyond 8 nm it shows itself in our image with a reflectance higher than a water droplet, i.e., the color of thin-film larger than 8 nm is slightly brighter than water droplets in the recorded images. As noted, it is not possible to accurately measure film larger than 8 nm with the current setting of SPRi. We can only comment whether a film with a thickness larger than 8 nm exist on the surface. The thickness of this film can be anything between 8 to 250 nm. **Error! Not a valid bookmark self-reference.** (b) and (c) show respectively the raw and processed image from stage III of UDC. In the raw image, the area between droplets has brighter color comparing to the color of droplets. In the processed image, droplets represent by dark blue, areas with thickness larger than 8 nm are identified with yellow color, and areas with thickness less than 8 nm have a bright blue color. Online Resource 3 is the video from stage III of UDC.

Figure 5.7 (a) Correlation between reflectance and thickness of water film for SPRi at experimental angle of 43.15 degrees and wavelength of 680 nm, (b) raw image of the thin film between droplets during UDC (dark gray and bright gray represent water and thin film respectively), and (c) processed image of the thin film grows between droplets during UDC (dark blue, light blue, and yellow color respectively represent droplet, film with thickness smaller than 8 nm, and film with thickness larger than 8 nm)

Figure 5.8 shows the time-lapse images of coalescence during stage III of UDC. It can be observed that after the coalescence, the swept area on the surface is not dry. In the example case of Figure 5.8, the thickness of swept area just after the coalescence increases beyond 8 nm, i.e., the reflectance of this area is higher than the reflectance of a droplet. Then, reflectance drops to a value lower than the reflectance of a droplet, i.e., the thickness of film becomes smaller than 8 nm. This fluctuation in thickness of film may be an indicator of the thin film instability or lateral transition of water molecules in the thin film. Figure 5.8 (d) shows the new droplets emerging on the surface after 42 ms from the start of coalescence. Online Resource 4 is the video of the droplet coalescence illustrated in Figure

5.8. Our results on UDC confirm findings of Song et al. [21] regarding the presence of thin-film larger than a monolayer between droplets.
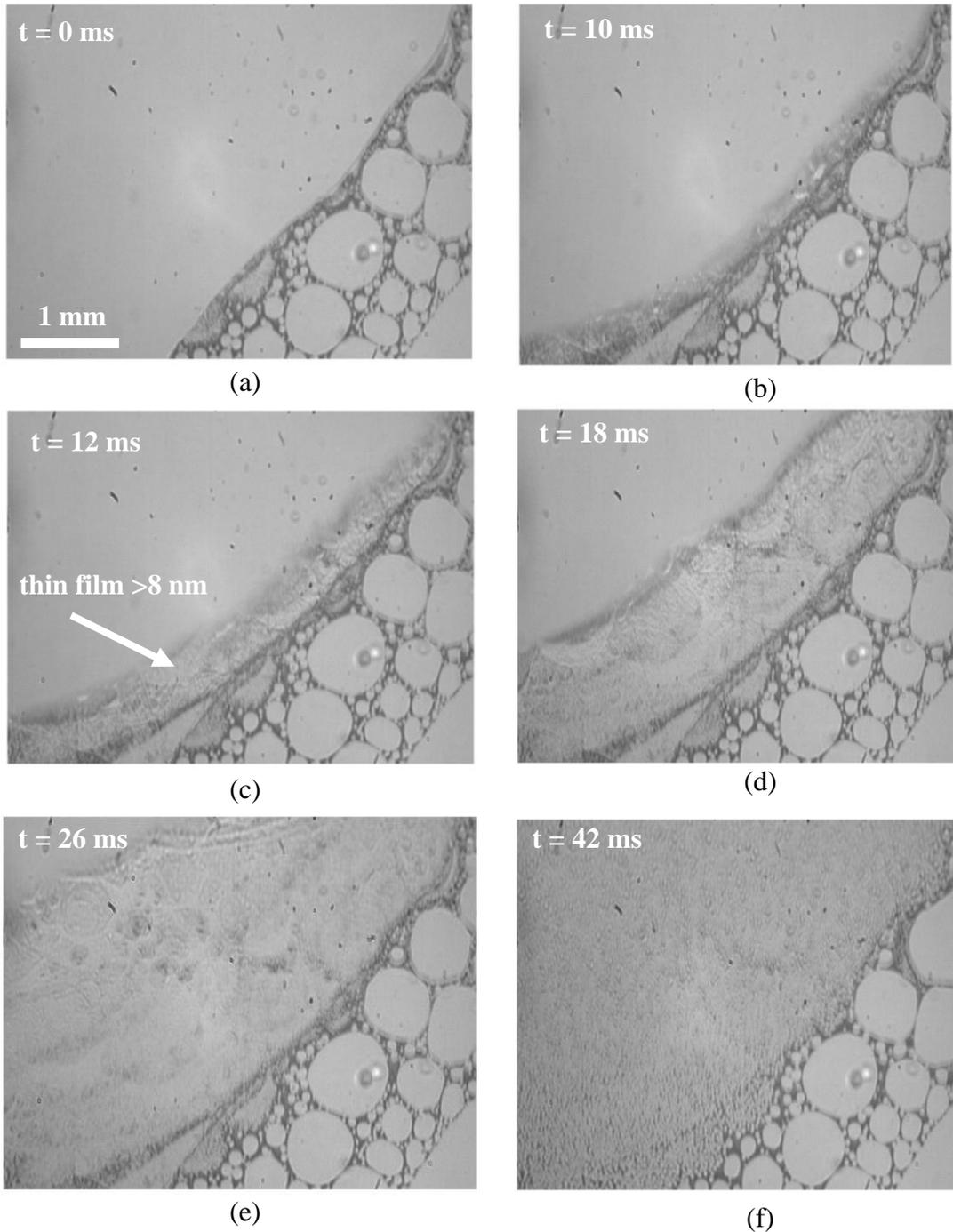

(a)

(b)

(c)

(d)

(e)

(f)

Figure 5.8 Time lapse images of coalescence during stage III og UDC shows presence of a thin film (> 8nm) at the exposed area and the subsequent film rupture.

5.3 Conclusion

The current work studied the mechanism of dropwise condensation on a smooth hydrophilic surface using SPRi. SPRi is a perfect tool to study thin film evolution as it can monitor dynamic changes of a thin film as small as 0.1 nm to 8 nm at a temporal resolution of 200-10,000 FPS. We studied two cases of dropwise condensation: SDC and UDC. In the case of SDC on a smooth hydrophilic gold surface, our studies showed no film larger than a monolayer form on the surface before the formation of initial droplets. Therefore, the droplets form on the surface at heterogeneous nucleation sites. The result confirms the findings of Umur and Griffith [23] fand other researchers in support of nucleation theory as the mechanism governing dropwise condensation. In the case of UDC where long-term dropwise condensation becomes unsustainable on the surface, visualization results showed a thin film with thickness larger than a monolayer grows between the droplets. We were able to detect thin-film thicker than 8 nm between the droplets during UDC. The finding on UDC confirms the finding of Song et al. [21] on the presence of a thin film between droplets during dropwise condensation of steam on a steel surface. In summary, our results show nucleation theory or film rupture theory cannot individually explain the mechanism of dropwise condensation. There is a need for a more comprehensive theory to explain the physics of dropwise condensation. Future work needs to quantitatively study the parameters affecting the growth of thin-film between droplets and the effect of thin-film on heat transfer rate.

6 Conclusion

Dropwise condensation has been under debate for the past nine decades. There are two competing theories on the mechanism of dropwise condensation: film rupture and nucleation theories. Research on dropwise condensation over the past century has yielded conflicting experimental results. These conflicting results have complicated understanding of the mechanism of dropwise condensation [19-23]. There are several ambiguities about the dropwise condensation mechanism such as:

- How do the initial droplets form on the substrate at the onset of condensation?
- What are the factors affecting droplet growth immediately after nucleation?
- Does a thin film exist between discrete droplets?
- Does the area between droplets participate in the overall surface heat transfer?

As these ambiguities are related to the existence and thickness of thin film on the substrate, we developed an automated super-resolution SPRi (with a lateral resolution of 4-10 µm, thickness resolution of 0.1-1 nm, and temporal resolution of 200-10,000 FPS) to thoroughly study the mechanism of dropwise condensation. In chapter 2, two methods to increase the temporal resolution of SPRi with IM are discussed. The temporal resolution of SPRi is increased up to 10,000 FPS by shortening the illumination path and broadening the bandpass filter from 10 FWHM to 60 FWHM. The SPRI with 10,000 FPS was used to record three stages – bridge formation, contact line motion, and relaxation of droplet – of coalescence during dropwise condensation.

In chapter 3, the development of automated angle-scanning SPRi was discussed. The developed microscope can perform angle scanning at a range of 40.0 to 80.0 degrees, which is suitable for sensing a variety of gases and fluids. In this chapter, we experimentally and theoretically showed the SPR signal dependence on temperature is less than 1% when the temperature changes from 25 °C to 70 °C. Also, we studied the probability of noise in the imaging and uncertainty in measuring a thin film. Our observation of the area between droplets during stable dropwise condensation showed the presence of a thin film with a thickness of one monolayer. This finding matches with the work of Umur and Griffith [23] in support of nucleation theory as the mechanism of dropwise condensation.

In chapter 4, the effect of adsorbed VOCs layer that forms on the surface during the dropwise condensation experiment was measured experimentally. The results indicate the adsorption of VOCs causes less than 30 % error in measurement of a monolayer water film that is observed between the droplets during the dropwise condensation on a gold-coated glass.

In chapter 5, SDC and UDC have been conducted on a smooth hydrophilic surface. The SDC conducted at the droplet growth rate of 1 µm/s in diameter showed the droplets form by nucleation at the onset of droplet condensation. The result confirms the results of previous experimental works [23] in support of nucleation theory. The results of UDC indicate the presence of thin film with a thickness of 8 nm or more between droplets during dropwise condensation. This data also confirms finding of Song et al. [21] on the presence

of a thin film between droplets. This work suggests neither nucleation theory nor film rupture theory can explain all scenarios occurring during dropwise condensation. These theories can be true in special experimental conditions. However, there is a need for a more comprehensive theory to explain the physics of dropwise condensation.

7 Reference List

[1]   S. B. Ahangar, V. Konduru, J. S. Allen, N. Miljkovic, S. H. Lee, and C. K. Choi, "Development of automated angle-scanning, high-speed surface plasmon resonance imaging and SPRi visualization for the study of dropwise condensation," *Experiments in Fluids,* vol. 61, no. 1, p. 12, 2019/12/03 2019, doi: 10.1007/s00348-019-2844-9.

[2]   S. Bayani, Y. Tabe, Y. T. Kang, S. H. Lee, and C. K. Choi, "Surface plasmon resonance imaging of drop coalescence at high-temporal resolution," *Journal of Flow Visualization and Image Processing,* vol. 25, no. 3-4, pp. 191-205, 2018.

[3]   S. B. Ahangar, C. H. Jeong, F. Long, J. S. Allen, S. H. Lee, and C. K. Choi, "The Effect of Adsorbed Volatile Organic Compounds on an Ultrathin Water Film Measurement," *Applied Sciences,* vol. 10, no. 17, p. 5981, 2020. [Online]. Available: https://www.mdpi.com/2076-3417/10/17/5981.

[4]   J. M. Beér, "High efficiency electric power generation: The environmental role," *Progress in Energy and Combustion Science,* https://doi.org/10.1016/j.pecs.2006.08.002 vol. 33, no. 2, pp. 107-134, 2007.

[5]   K. Daou, R. Wang, and Z. Xia, "Desiccant cooling air conditioning: a review," *Renewable and Sustainable Energy Reviews,* vol. 10, no. 2, pp. 55-77, 2006.

[6]   S. G. Kandlikar and Z. Lu, "Thermal management issues in a PEMFC stack – A brief review of current status," *Applied Thermal Engineering,* https://doi.org/10.1016/j.applthermaleng.2008.05.009 vol. 29, no. 7, pp. 1276-1280, 2009.

[7]   M. Rahim-Esbo, S. Bayani, R. Mohammadyari, A. K. Asboei, S. Mohsenian, and S. E. Mousavitileboni, "Analytical and Numerical investigation of natural convection in a heated cylinder using Homotopy Perturbation Method," *Acta Scientiarum. Technology,* vol. 36, no. 4, pp. 669-677, 2014.

[8]   I. Tanasawa, "Advances in condensation heat transfer," in *Advances in Heat Transfer Volume 21*: Elsevier, 1991, pp. 55-139.

[9]   E. Schmidt, W. Schurig, and W. Sellschopp, "Condensation of water vapour in film-and drop form," *Tech. Mech. Thermodyn,* vol. 1, pp. 53-63, 1930.

[10]   J. W. Rose, "Dropwise condensation theory and experiment: A review," *Proceedings of the Institution of Mechanical Engineers, Part A: Journal of Power and Energy,* https://doi.org/10.1243/09576500260049034 vol. 216, no. 2, pp. 115-128, 2002.

[11]   N. M. Nouri, S. Sekhavat, S. Bayani Ahangar, and N. Faal Nazari, "Effect of curing condition on superhydrophobic surface for 7075Al," *Journal of Dispersion Science and Technology,* vol. 33, no. 6, pp. 771-774, 2012.

[12]   H. Emonsi, "The mechanism of dropwise condensation," *American Institute of Chemical Engineers, Trans,* vol. 35, pp. 109-125, 1939.

[13]   N. Miljkovic and E. N. Wang, "Condensation heat transfer on superhydrophobic surfaces," *MRS bulletin,* vol. 38, no. 5, pp. 397-406, 2013.

[14]   H. J. Cho, D. J. Preston, Y. Zhu, and E. N. Wang, "Nanoengineered materials for liquid–vapour phase-change heat transfer," *Nature Reviews Materials,* vol. 2, no. 2, p. 16092, 2017.

[15]   R. Enright, N. Miljkovic, J. L. Alvarado, K. Kim, and J. W. Rose, "Dropwise condensation on micro-and nanostructured surfaces," *Nanoscale and Microscale Thermophysical Engineering,* vol. 18, no. 3, pp. 223-250, 2014/07/03 2014, doi: 10.1080/15567265.2013.862889.

[16]   M. Ahlers, A. Buck-Emden, and H.-J. Bart, "Is dropwise condensation feasible? A review on surface modifications for continuous dropwise condensation and a profitability analysis," *Journal of Advanced Research,* vol. 16, pp. 1-13, 2018.

[17]   J. Oh, R. Zhang, P. P. Shetty, J. A. Krogstad, P. V. Braun, and N. Miljkovic, "Thin film condensation on nanostructured surfaces," *Advanced Functional Materials,* vol. 28, no. 16, p. 1707000, 2018.

[18]   J. Ma, H. Cha, M.-K. Kim, D. G. Cahill, and N. Miljkovic, *Advanced Functional Materials,* 2019.

[19]   G. Tammann and W. J. A. d. P. Boehme, "Die Zahl der Wassertröpfchen bei der Kondensation auf verschiedenen festen Stoffen," vol. 414, no. 1, pp. 77-80, 1935.

[20]   J. L. McCormick and E. Baer, "On the mechanism of heat transfer in dropwise condensation," *Journal of Colloid Science,* https://doi.org/10.1016/0095-8522(63)90012-6 vol. 18, no. 3, pp. 208-216, 1963.

[21]   S. Yongji, X. Dunqi, L. Jifang, T. J. I. j. o. h. Siexong, and m. transfer, "A study on the mechanism of dropwise condensation," vol. 34, no. 11, pp. 2827-2831, 1991.

[22]   A. Majumdar and I. Mezic, "Instability of ultra-thin water films and the mechanism of droplet formation on hydrophilic surfaces," *Journal of heat transfer,* vol. 121, no. 4, pp. 964-971, 1999.

[23]   A. Umur and P. Griffith, "Mechanism of Dropwise Condensation," *Journal of Heat Transfer,* https://doi.org/10.1115/1.3689090 vol. 87, no. 2, pp. 275-275, 1965.

[24]   M. Jakob, *Heat transfer in evaporation and condensation*. Urbana, Ill: University of Illinois, 1937.

[25]   S. Yongji, X. Dunqi, L. Jifang, and T. Siexong, "A study on the mechanism of dropwise condensation," *International Journal of Heat and Mass Transfer,* vol. 34, no. 11, pp. 2827-2831, 1991.

[26]   G. Tammann and W. Boehme, "Die zahl der wassertröpfchen bei der kondensation auf verschiedenen festen etoffen," *Annalen der Physik,* vol. 414, no. 1, pp. 77-80, 1935.

[27]   S. Khandekar and K. Muralidhar, "Modeling dropwise condensation," in *Dropwise Condensation on Inclined Textured Surfaces*: Springer, 2014, pp. 17-72.

[28]   F. Chu, X. Wu, Y. Zhu, and Z. Yuan, "Relationship between condensed droplet coalescence and surface wettability," *International Journal of Heat and Mass Transfer,* https://doi.org/10.1016/j.ijheatmasstransfer.2017.04.052 vol. 111, pp. 836-841, 2017.

[29] M. A. Nilsson and J. P. Rothstein, "The effect of contact angle hysteresis on droplet coalescence and mixing," *Journal of Colloid and Interface Science,* vol. 363, no. 2, pp. 646-654, 2011.

[30] Z. Barkay, "In situ imaging of nano-droplet condensation and coalescence on thin water films," *Microscopy and Microanalysis,* https://doi.org/10.1017/s1431927613013834 vol. 20, no. 02, pp. 317-322, 2013.

[31] S. Anand and S. Y. Son, "Sub-micrometer dropwise condensation under superheated and rarefied vapor condition," *Langmuir,* https://doi.org/10.1021/la102642r vol. 26, no. 22, pp. 17100-17110, 2010.

[32] C. S. Sharma, J. Combe, M. Giger, T. Emmerich, and D. Poulikakos, "Growth rates and spontaneous navigation of condensate droplets through randomly structured textures," *ACS Nano,* https://doi.org/10.1021/acsnano.6b07471 vol. 11, no. 2, pp. 1673-1682, 2017.

[33] K. Rykaczewski, J. H. J. Scott, S. Rajauria, J. Chinn, A. M. Chinn, and W. Jones, "Three dimensional aspects of droplet coalescence during dropwise condensation on superhydrophobic surfaces," *Soft Matter,* https://doi.org/10.1039/c1sm06219k vol. 7, no. 19, pp. 8749-8749, 2011.

[34] H. Cha *et al.*, "Coalescence-induced nanodroplet jumping," *Physical Review Fluids,* vol. 1, no. 6, p. 064102, 2016.

[35] X. Zhang, P. Tchoukov, R. Manica, L. Wang, Q. Liu, and Z. Xu, "Simultaneous measurement of dynamic force and spatial thin film thickness between deformable and solid surfaces by integrated thin liquid film force apparatus," *Soft matter,* vol. 12, no. 44, pp. 9105-9114, 2016.

[36] C. K. Choi, C. H. Margraves, A. E. English, and K. D. Kihm, "Multicontrast microscopy technique to dynamically fingerprint live-cell focal contacts during exposure and replacement of a cytotoxic medium," *Journal of biomedical optics,* vol. 13, no. 5, p. 054069, 2008.

[37] I. I. Kim, S. Paik, Y. B. Jeon, J. S. Park, H. Kim, and H. Kim, "Full-field thickness measurement of ultrathin liquid film in receding contact-induced nano-channel using surface plasmon resonance," *Optics express,* vol. 26, no. 16, pp. 20975-20989, 2018.

[38] S. Bayani Ahangar, K. Bellur, E. Medici, K. Tajiri, J. S. Allen, and C. K. Choi, "Surface plasmon resonance imaging: an inexpensive tool to study the water transport in thin film PFSA ionomers," *Meeting Abstracts,* vol. MA2019-02, no. 54, p. 2312, September 1, 2019 2019. [Online]. Available: http://ma.ecsdl.org/content/MA2019-02/54/2312.abstract.

[39] K. Rykaczewski, S. Anand, S. B. Subramanyam, and K. K. Varanasi, "Mechanism of frost formation on lubricant-Impregnated surfaces," *Langmuir,* https://doi.org/10.1021/la400801s vol. 29, no. 17, pp. 5230-5238, 2013.

[40] L. Zhang *et al.*, "Enhanced environmental scanning electron microscopy using phase reconstruction and Its application in condensation," *ACS Nano,* vol. 13, no. 2, pp. 1953-1960, 2019/02/26 2019, doi: 10.1021/acsnano.8b08389.

[41] J. Plawsky *et al.*, "Nano-and microstructures for thin-film evaporation—A review," *Nanoscale and microscale thermophysical engineering,* vol. 18, no. 3, pp. 251-269, 2014.

[42]   Z. Li *et al.*, "Low-temperature growth of graphene by chemical vapor deposition using solid and liquid carbon sources," *ACS nano,* vol. 5, no. 4, pp. 3385-3390, 2011.

[43]   C. W. Lo, C. C. Wang, and M. C. Lu, "Spatial control of heterogeneous nucleation on the superhydrophobic nanowire array," *Advanced Functional Materials,* vol. 24, no. 9, pp. 1211-1217, 2014.

[44]   A. Steele, I. Bayer, and E. Loth, "Inherently superoleophobic nanocomposite coatings by spray atomization," *Nano letters,* vol. 9, no. 1, pp. 501-505, 2008.

[45]   K. Rykaczewski, T. Landin, M. L. Walker, J. H. J. Scott, and K. K. Varanasi, "Direct imaging of complex nano-to microscale interfaces involving solid, liquid, and gas phases," *ACS nano,* vol. 6, no. 10, pp. 9326-9334, 2012.

[46]   T. Fukuma *et al.*, "Mechanism of atomic force microscopy imaging of three-dimensional hydration structures at a solid-liquid interface," *Physical Review B,* vol. 92, no. 15, p. 155412, 2015.

[47]   A. Ciesielski, M. El Garah, S. Haar, P. Kovaříček, J.-M. Lehn, and P. Samorì, "Dynamic covalent chemistry of bisimines at the solid/liquid interface monitored by scanning tunnelling microscopy," *Nature chemistry,* vol. 6, no. 11, p. 1017, 2014.

[48]   K. Bellur *et al.*, "Visualization of the evaporation and condensation phenomena in cryogenic propellants," *Journal of Flow Visualization and Image Processing,* vol. 23, no. 1-2, 2016.

[49]   T. T. Goodrich, H. J. Lee, and R. M. Corn, "Direct detection of genomic DNA by enzymatically amplified SPR imaging measurements of RNA microarrays," *Journal of the American Chemical Society,* vol. 126, no. 13, pp. 4086-4087, 2004.

[50]   K. D. Kihm, *Near-field characterization of micro/nano-scaled fluid flows.* Springer Science & Business Media, 2011.

[51]   I. T. Kim and K. D. Kihm, "Real-time and full-field detection of near-wall salinity using surface plasmon resonance reflectance," *Analytical chemistry,* vol. 79, no. 14, pp. 5418-5423, 2007.

[52]   D. J. Graham and L. R. Watkins, "Surface plasmon resonance imaging with polarisation modulation," in *Sensors, 2009 IEEE*, 2009: IEEE, pp. 1997-2000.

[53]   C. H. Jeong, D. H. Shin, V. Konduru, J. S. Allen, C. K. Choi, and S. H. Lee, "Quantitative measurements of nanoscale thin frost layers using surface plasmon resonance imaging," *International Journal of Heat and Mass Transfer,* vol. 124, pp. 83-89, 2018.

[54]   C. H. Jeong, S. H. Lee, D. H. Shin, V. Konduru, J. S. Allen, and C. K. Choi, "High Speed SPR Visualization of Frost Propagation Inside a Subcooled Water Droplet," *Journal of Heat Transfer,* vol. 139, no. 2, p. 020905, 2017.

[55]   V. Konduru *et al.*, "High-Speed Surface Plasmon Resonance (SPR) Reflectance Imaging of Drop Coalescence during Condensation and Evaporation," *Journal of Heat Transfer,* vol. 138, no. 8, p. 080903, 2016.

[56]   M. Yamamoto, "Surface plasmon resonance (SPR) theory: tutorial," *Review of Polarography,* vol. 48, no. 3, pp. 209-237, 2002.

[57]   Y. Zeng *et al.*, "Recent advances in surface plasmon resonance imaging: detection speed, sensitivity, and portability," *Nanophotonics,* vol. 6, no. 5, pp. 1017-1030, 2017.

[58]   M. R. Hoque and M. Rashed-Al-Mahfuz, "A new approach in spatial filtering to reduce speckle noise," *International Journal of Soft Computing and Engineering (IJSCE),* vol. 1, no. 3, pp. 29-32, 2011.

[59]   M. C. Pierce, B. H. Park, B. Cense, and J. F. de Boer, "Simultaneous intensity, birefringence, and flow measurements with high-speed fiber-based optical coherence tomography," *Optics letters,* vol. 27, no. 17, pp. 1534-1536, 2002.

[60]   L. Wang, G. Zhang, H. Wu, J. Yang, and Y. Zhu, "Note: A top-view optical approach for observing the coalescence of liquid drops," *Review of Scientific Instruments,* vol. 87, no. 2, p. 026103, 2016.

[61]   K. Daou , R. Wang, and Z. Xia, "Desiccant cooling air conditioning: a review," *Renewable and Sustainable Energy Reviews,* https://doi.org/10.1016/j.rser.2004.09.010 vol. 10, no. 2, pp. 55-77, 2006.

[62]   T.-C. Hung, T. Shai, and S. K. Wang, "A review of organic Rankine cycles (ORCs) for the recovery of low-grade waste heat," *Energy,* vol. 22, no. 7, pp. 661-667, 1997.

[63]   W. Castle, "Air separation and liquefaction: recent developments and prospects for the beginning of the new millennium," *International Journal of Refrigeration,* vol. 25, no. 1, pp. 158-172, 2002.

[64]   A. T. Paxson, J. L. Yagüe, K. K. Gleason, and K. K. Varanasi, "Stable dropwise condensation for enhancing heat transfer via the initiated chemical vapor deposition (iCVD) of grafted polymer films," *Advanced Materials,* vol. 26, no. 3, pp. 418-423, 2014.

[65]   V. P. Carey, *Liquid vapor phase change phenomena: an introduction to the thermophysics of vaporization and condensation processes in heat transfer equipment*. CRC Press, 2018.

[66]   R. Webb and N. Kim, "Principles of Enhanced Heat Transfer, Taylor & Francis," *New York,* vol. 108, 2005.

[67]   V. Konduru *et al.*, "High-Speed Surface Plasmon Resonance (SPR) Reflectance Imaging of Drop Coalescence during Condensation and Evaporation," *Journal of Heat Transfer,* https://doi.org/10.1115/1.4033819 vol. 138, no. 8, pp. 080903-080903, 2016.

[68]   M. Ahlers, A. Buck-Emden, and H.-J. Bart, "Is dropwise condensation feasible? A review on surface modifications for continuous dropwise condensation and a profitability analysis," *Journal of Advanced Research,* 2018.

[69]   A. Leipertz, "J3 dropwise condensation," in *VDI Heat Atlas*: Springer, 2010, pp. 933-938.

[70]   C. H. Jeong, S. H. Lee, D. H. Shin, V. Konduru, J. S. Allen, and C. K. Choi, "High speed SPR visualization of frost propagation inside a subcooled water droplet," *J Heat Trans,* https://doi.org/10.1115/1.4035575 vol. 139, no. 2, pp. 020905-020905, 2017.

[71]   J. Homola, "Present and future of surface plasmon resonance biosensors," *Analytical and bioanalytical chemistry,* https://doi.org/10.1007/s00216-003-2101-0 vol. 377, no. 3, pp. 528-539, 2003.

[72]   J. Homola, "Surface plasmon resonance sensors for detection of chemical and biological species," *Chemical Reviews,* https://doi.org/10.1021/cr068107d vol. 108, no. 2, pp. 462-493, 2008.

[73]   B. Rothenhäusler and W. Knoll, "Surface–plasmon microscopy," *Nature,* https://doi.org/10.1038/332615a0 vol. 332, no. 6165, pp. 615-617, 1988.

[74]   S. Bayani Ahangar, K. Bellur, E. Medici, K. Tajiri, J. S. Allen, and C. K. Choi, "optical properties and swelling of thin Film perfluorinated sulfonic-acid ionomer," *ECS Transactions,* vol. 92, no. 8, pp. 197-204, July 3, 2019 2019, doi: 10.1149/09208.0197ecst.

[75]   L. K. Wolf, Y. Gao, and R. M. Georgiadis, "Kinetic siscrimination of sequence-specific DNA-drug binding measured by surface plasmon resonance Imaging and comparison to solution-phase measurements," *Journal of the American Chemical Society,* https://doi.org/10.1021/ja072401l vol. 129, no. 34, pp. 10503-10511, 2007.

[76]   K. D. Kihm, "Surface plasmon resonance reflectance imaging technique for near-field (~ 100 nm) fluidic characterization," *Experiments in fluids,* vol. 48, no. 4, pp. 547-564, 2010.

[77]   E. Kretschmann and H. Raether, "Radiative decay of non radiative surface plasmons excited by light," *Zeitschrift für Naturforschung A,* https://doi.org/10.1515/zna-1968-1247 vol. 23, no. 12, pp. 2135-2136, 1968.

[78]   L.-l. Zhang, X. Chen, and D.-f. Cui, "Performance of surface plasmon resonance imaging system based on angular modulation and intensity measurement," *Optoelectronics Letters,* https://doi.org/10.1007/s11801-016-5247-7 vol. 12, no. 3, pp. 226-228, 2016.

[79]   H. E. de Bruijn, R. P. H. Kooyman, and J. Greve, "Surface plasmon resonance microscopy: improvement of the resolution by rotation of the object," *Applied Optics,* https://doi.org/10.1364/ao.32.002426 vol. 32, no. 13, pp. 2426-2426, 1993.

[80]   Y. Zeng *et al.*, "Recent advances in surface plasmon resonance imaging: detection speed, sensitivity, and portability," *Nanophotonics,* https://doi.org/10.1515/nanoph-2017-0022 vol. 6, no. 5, pp. 1017-1030, 2017.

[81]   J. B. Beusink, A. M. C. Lokate, G. A. J. Besselink, G. J. M. Pruijn, and R. B. M. Schasfoort, "Angle-scanning SPR imaging for detection of biomolecular interactions on microarrays," *Biosensors and Bioelectronics,* https://doi.org/10.1016/j.bios.2007.08.025 vol. 23, no. 6, pp. 839-844, 2008.

[82]   J. A. Ruemmele *et al.*, "Quantitative Surface Plasmon Resonance Imaging: A Simple Approach to Automated Angle Scanning," *Analytical Chemistry,* https://doi.org/10.1021/ac702544q vol. 80, no. 12, pp. 4752-4756, 2008.

[83]   C. Zhou *et al.*, "An angle-scanning surface plasmon resonance imaging device for detection of mismatched bases in caspase-3 DNA," *Analytical Methods,* https://doi.org/10.1039/c3ay26602h vol. 5, no. 9, pp. 2369-2369, 2013.

[84]   B. Afkhami, Y. Wang, S. A. Miers, and J. D. Naber, "Experimental determination of flame speed and flame stretch using an optically accessible, spark-ignition engine," *International Journal of Engine Research,* 2019, doi: https://doi.org/10.1177/1468087419877718.

[85]   S. W. Hasinoff, "Photon, Poisson noise," in *Computer Vision: A Reference Guide*, K. Ikeuchi Ed. Boston, MA: Springer, 2014, pp. 608-610.

[86]   I. T. Kim and K. D. Kihm, "Label-free visualization of microfluidic mixture concentration fields using a surface plasmon resonance (spr) reflectance imaging," *Experiments in fluids,* vol. 41, no. 6, pp. 905-916, 2006.

[87]   M. Yamamoto, "Surface plasmon resonance (SPR) theory: tutorial," *Review of Polarography*

vol. 48, no. 3, pp. 209-237, 2002.

[88]   H. Chiang *et al.*, "Effects of temperature on the surface plasmon resonance at a metal–semiconductor interface," *Thin Solid Films,* vol. 515, no. 17, pp. 6953-6961, 2007.

[89]   I. T. Kim and K. D. Kihm, "Full-field and real-time surface plasmon resonance imaging thermometry," *Optics Letters,* vol. 32, no. 23, pp. 3456-3458, 2007/12/01 2007, doi: 10.1364/OL.32.003456.

[90]   M. Englert, P. Hartmann, and S. Reichel, *Optical glass: refractive index change with wavelength and temperature* (SPIE Photonics Europe). SPIE, 2014.

[91]   A. Alabastri *et al.*, "Molding of plasmonic resonances in metallic nanostructures: Dependence of the non-linear electric permittivity on system size and temperature," *Materials,* vol. 6, no. 11, pp. 4879-4910, 2013.

[92]   A. N. Bashkatov and E. A. Genina, *Water refractive index in dependence on temperature and wavelength: a simple approximation* (Saratov Fall Meeting 2002 Laser Physics and Photonics, Spectroscopy, and Molecular Modeling III; Coherent Optics of Ordered and Random Media III). SPIE, 2003.

[93]   D. Orejon, A. Askounis, Y. Takata, and D. Attinger, "Dropwise condensation on multi-scale bioinspired metallic surfaces with nano-features," *ACS applied materials & interfaces,* 2019.

[94]   D. J. Preston, N. Miljkovic, J. Sack, R. Enright, J. Queeney, and E. N. Wang, "Effect of hydrocarbon adsorption on the wettability of rare earth oxide ceramics," *Applied Physics Letters,* vol. 105, no. 1, p. 011601, 2014.

[95]   X. Yan *et al.*, "Atmosphere-mediated superhydrophobicity of rationally designed micro/nanostructured surfaces," *ACS nano,* vol. 13, no. 4, pp. 4160-4173, 2019.

[96]   H. Cha, A. Wu, M.-K. Kim, K. Saigusa, A. Liu, and N. Miljkovic, "Nanoscale-agglomerate-mediated heterogeneous nucleation," *Nano letters,* vol. 17, no. 12, pp. 7544-7551, 2017.

[97]   S. Chavan *et al.*, "Heat transfer through a condensate droplet on hydrophobic and nanostructured superhydrophobic surfaces," *Langmuir,* vol. 32, no. 31, pp. 7774-7787, 2016/08/09 2016, doi: 10.1021/acs.langmuir.6b01903.

[98]   X. Yan *et al.*, "Hierarchical Condensation," *ACS nano,* vol. 13, no. 7, pp. 8169-8184, 2019.

[99]   K. Saga and T. Hattori, "Organic contamination control in silicon surface processing," in *Solid State Phenomena*, 2005, vol. 103: Trans Tech Publ, pp. 49-54.

[100] I. Langmuir, "Surface chemistry," *Chemical Reviewes,* vol. 13, no. 2, pp. 147-191, 1933.

[101] A. Umur and P. Griffith, "Mechanism of dropwise condensation," Cambridge, Mass.: MIT Dept. of Mechanical Engineering, 1963.

[102] S. Khandekar and K. Muralidhar, *Dropwise condensation on inclined textured surfaces*. New York: Springer, 2014, p. New York.

[103] X. Hu, Q. Yi, X. Kong, and J. Wang, "A Review of Research on Dropwise Condensation Heat Transfer," *Applied Sciences,* vol. 11, no. 4, p. 1553, 2021. [Online]. Available: https://www.mdpi.com/2076-3417/11/4/1553.

[104] Q. Sheng, J. Sun, Q. Wang, W. Wang, and H. S. Wang, "On the onset of surface condensation: formation and transition mechanisms of condensation mode," *Scientific Reports,* vol. 6, no. 1, p. 30764, 2016/08/02 2016, doi: 10.1038/srep30764.

[105] B. S. Sikarwar, S. Khandekar, S. Agrawal, S. Kumar, and K. Muralidhar, "Dropwise Condensation Studies on Multiple Scales," *Heat Transfer Engineering,* vol. 33, no. 4-5, pp. 301-341, 2012/03/01 2012, doi: 10.1080/01457632.2012.611463.

[106] S. B. Ahangar, J. S. Allen, S. H. Lee, and C. K. Choi, "Surface Plasmon Resonance Imaging: A Technique to Reveal the Dropwise Condensation Mechanism," *Journal of Heat Transfer,* vol. 142, no. 3, 2020, doi: 10.1115/1.4046136.

A   Copyright Permission

Figure A.1 Permission to reus material in Chapter 2.